Joonas Iivanainen

Active magnetic shield for optical neuromagnetic measurements

School of Science

Thesis submitted for examination for the degree of Master of Science in Technology.

Espoo 22.3.2016

Thesis supervisor and advisor:

Prof. Lauri Parkkonen

Aalto University
School of Science

AALTO UNIVERSITY
SCHOOL OF SCIENCE

ABSTRACT OF THE
MASTER'S THESIS

Author: Joonas Iivanainen

Title: Active magnetic shield for optical neuromagnetic measurements

Date: 22.3.2016 Language: English Number of pages: 6+58

Department of Neuroscience and Biomedical Engineering

Professorship: Biomedical Engineering

Supervisor and advisor: Prof. Lauri Parkkonen

Optically-pumped magnetometers, based on optical measurement of the magnetization of an alkali vapor, are emerging as a promising alternative sensor for recording magnetic fields generated by the human brain. These sensors can only operate at very low absolute magnetic fields and therefore efficient shielding against the ambient magnetic field is required. The standard in biomagnetism is to use a passive magnetically shielded room to obtain sufficient shielding; however, the remanent magnetic field in a typical shielded room often exceeds the limits of these new magnetometers.

In this thesis, a suitable ultra-low-field environment for the use of these sensors in Aalto University was set up. First, the magnetic fields inside the two- and three-layer magnetically shielded rooms of Aalto University were surveyed and then a portable active compensation system for further reducing the fields was built.

Without compensation, the measured remanent magnetic fields were on the order of 100 nT and 5 nT in the two- and three-layer rooms while the gradients were about 40 nT/m and 5 nT/m, respectively. Both rooms had low-frequency field drifts of approximately 1 nT in a measurement period of 200 s. With the constructed compensation coil set, the static field could be reduced by a factor of about 10 in a head-sized volume. The feedback loop of the compensation system was also capable of locking the field to zero at the sensor site and could also remove the low-frequency fluctuations in the field.

This study showed that neuromagnetic measurements with optically-pumped magnetometers should be feasible in standard shielded rooms by utilizing the constructed compensation system.

Keywords: magnetoencephalography, optically-pumped magnetometer, magnetic shielding, active compensation

AALTO-YLIOPISTO
PERUSTIETEIDEN KORKEAKOULU

DIPLOMITYÖN
TIIVISTELMÄ

Tekijä: Joonas Iivanainen

Työn nimi: Aktiivinen magneettinen suoja optisiin neuromagneettisiin mittauksiin

Päivämäärä: 22.3.2016 Kieli: Englanti Sivumäärä: 6+58

Neurotieteen ja lääketieteellisen tekniikan laitos

Professuuri: Lääketieteellinen tekniikka

Työn valvoja ja ohjaaja: Prof. Lauri Parkkonen

Optisesti pumpatut magnetometrit, jotka perustuvat alkalimetallikaasun magnetisaation optiseen mittaukseen, ovat lupaavia vaihtoehtoisia antureita ihmisaivojen synnyttämien magneettikenttien rekisteröimiseen. Nämä sensorit toimivat vain hyvin alhaisissa magneettikentissä, joten tehokkaita menetelmiä tarvitaan ympäröivältä magneettikentältä suojautumiseen. Tyypillisesti biomagneettisia kenttiä mitattaessa vaadittava suojaus on saatu käyttämällä passiivista magneettisesti suojattua huonetta; jäännöskenttä tyypillisen suojahuoneen sisällä kuitenkin ylittää optisten magnetometrien vaatimukset.

Tämän työn tarkoituksena oli luoda suotuisa magneettinen ympäristö Aalto-yliopistoon näiden anturien käyttöä varten. Ensiksi remanenssimagneettikentät Aallon kaksi- ja kolmikerrossuojahuoneissa mitattiin ja mallinnettiin, jonka perusteella suunniteltiin ja rakennettiin liikuteltava aktiivinen kompensointijärjestelmä näiden kenttien pienentämistä varten.

Mitatut remanenssikentät olivat suuruusluokaltaan 100 nT kaksikerroshuoneessa ja 5 nT kolmikerroshuoneessa; gradientit olivat vastaavasti noin 40 nT/m ja 5 nT/m. Kentän matalataajuiset fluktuaatiot olivat noin 1 nT:n luokkaa molemmissa huoneissa mittausajan ollessa 200 s. Rakennetulla kompensointijärjestelmällä suojahuoneiden staattinen kenttä pystyttiin pienentämään kymmenesosaan pään kokoisessa tilavuudessa. Järjestelmän takaisinkytkentäsilmukka pystyi nollaamaan kentän anturin kohdassa ja poistamaan matalataajuiset häiriöt kentästä.

Tämä työ osoitti, että rakennettua kompensointijärjestelmää käyttämällä optisesti pumpatuilla magnetometreillä voidaan tehdä herkkiä neuromagneettisia mittauksia tyypillisissä magneettisesti suojatuissa huoneissa.

Avainsanat: magnetoenkefalografia, optisesti pumpattu magnetometri, magneettinen suojaus, aktiivinen kompensointi

Preface

I have always been wondering whether the supervisor and advisor review the preface of the thesis or is it just a piece of text that is left as it was originally written by the author. I shall soon find the answer to this question as I return the draft of this thesis to my supervisor. The readers, however, will not get the answer just by reading this as the content of the preface will not (presumably) change whether the supervisor reviews it or not. If the language of the preface is not corrected by the supervisor or advisor, what does it tell from the author if the preface is full of poor language and spelling mistakes while the rest of the thesis is seemingly well-written? Are you even allowed to write anything you want to the preface? Oh well, I guess that this is the part of the thesis where you have to thank everyone...

I think that it is not wise to thank people by names in the preface of your thesis or anywhere because you always forget someone and those people get upset as they look for their name from the long lists without success. So I want to thank everyone who has been involved in my life during my studies. However, there are some people who deserve their name to be mentioned here (it is kind of conflicting that after saying the above I want to name particular persons). First, I want to thank my supervisor Lauri for introducing me to the field of biomagnetism by taking me first as a summer student to the lab several years ago and then by allowing me to work in the lab. I am also grateful for the responsibilities and interesting assignments you have given me. It has always been a pleasure to work in the lab and with you. I also want to express my deepest gratitude to my parents, Eeva and Pauli, and to my sister Janica. You are the ones that provided the background and support that enabled this thesis, my studies and my whole life, basically.

I will always remember how my mother made me do simple calculations during the bed time when I was a kid (these are some of the earliest memories I have). 'How much is two plus four?' she asked. Then I counted it with my fingers and answered, 'Six.' 'Correct,' said mom and I was satisfied. Then my father would jokingly ask, 'How much is seven plus four?' And, oh boy, I ran out of fingers! I was very confused and curious. I think that these events made some kind of impact on me. They must have triggered my scientific curiousity and certainly play a role in my choice to study physics and mathematics.

Otaniemi, 22.3.2016

Joonas Iivanainen

Contents

Operators and abbreviations

Operators

$\nabla\phi$	gradient of ϕ
$\nabla \cdot \mathbf{A}$	divergence of vector $\mathbf{A}$
$\nabla \times \mathbf{A}$	curl of vector $\mathbf{A}$
$\nabla^2\phi$	Laplacian of ϕ
$\frac{\mathrm{d}}{\mathrm{d}t}$	derivative with respect to variable t
$\frac{\partial}{\partial t}$	partial derivative with respect to variable t
$\int_V \phi dV$	integral of ϕ over volume V
$\int_S \mathbf{A} \cdot \mathbf{dS}$	integral of $\mathbf{A}$ over surface S
$\sum_i$	sum over index i
$\prod_i$	product over index i
$\mathbf{A} \cdot \mathbf{B}$	dot product of vectors $\mathbf{A}$ and $\mathbf{B}$
$\mathbf{A} \times \mathbf{B}$	cross product of vectors $\mathbf{A}$ and $\mathbf{B}$
$\|\|\mathbf{A}\|\|$	Euclidean norm of vector $\mathbf{A}$
$[a, b]$	commutator of a and b
$\langle A \rangle$	expectation value of A
$\mathrm{Tr}(A)$	trace of A

Abbreviations

AC	alternating current
ADC	analog-to-digital converter
BEM	boundary element method
CSOPM	chip-scale optically-pumped magnetometer
DC	direct current
DF	direct-form
DFIIt	direct-form II transposed
DSP	digital signal processor
EEG	electroencephalography
IIR	infinite impulse response
ISA	isolated source approach
MEG	magnetoencephalography
MEMS	microelectromechanical systems
MSR	magnetically shielded room
OPM	optically-pumped magnetometer
RMS	root mean square
RMSE	root-mean-square error
SCSI	small computer system interface
SERF	spin exchange relaxation-free
SQUID	superconducting quantum interference device

1 Introduction

Magnetoencephalography (MEG) is a non-invasive neuroimaging technique that relies on detecting the weak extracranial magnetic fields generated by neural currents [1, 2]. Due to the weakness of these fields, highly sensitive magnetic field sensors and sophisticated magnetic noise cancellation methods are needed. To date, superconducting quantum interference devices (SQUIDs) have been the only sensors with an adequate sensitivity to enable practical whole-scalp mappings of the extracerebral neuromagnetic fields. In addition, they are suitable for mass-manufacturing and thus form the basis of the commercial state-of-the-art MEG devices.

However, as the name implies, SQUIDs require a cryogenic environment for their operation, and thus they are typically cooled with liquid helium (boiling point 4.2 K) to a low-enough temperature. The necessity of liquid-helium cooling and thus also cryogenic equipment impose major constraints on the current MEG systems. First, liquid helium is a scarce and expensive natural resource, whose availability fluctuates. Second, the needed cryogenic equipment are bulky, making the whole device inconveniently large. Third, the necessary thermal isolation around the cryogenic environment imposes a lower limit, typically about 2 cm, on the distance from the sensors to the subject's scalp. Last, the sensor array of a SQUID-based MEG system is not adjustable to each individual's head shape and size. The last two issues also limit the signal-to-noise ratio and spatial resolution achievable with the current MEG sensor arrays.

Recent advances in optical magnetometry [3, 4] indicate that optically-pumped, or atomic, magnetometers (OPMs) could be a feasible, non-cryogenic alternative to SQUIDs for biomagnetic measurements as OPMs are approaching [5, 6] and even surpassing [7] SQUIDs in sensitivity. Additionally, chip-scale microfabricated optically-pumped magnetometers [8] have dimensions suitable for multichannel whole-scalp-covering MEG sensor arrays and these sensors could be also placed within few millimetres from the subject's scalp. Thus, with the chip-scale OPMs, MEG could be measured with EEG-cap-like sensor arrays. Further, several studies have proved the feasibility of OPMs for recording biomagnetic signals (see Refs. 5, 6, 8, 9 and 10, for example). Taking these facts into account, it is no surprise that OPMs have attracted considerable interest in the community of bioelectromagnetism.

The adaptation of the OPMs to neuroscience does not happen without effort. The detection of the weak neuromagnetic fields requires proper shielding from the static and dynamic magnetic fields generated by environmental noise sources (e.g., cars, elevators, the geomagnetic field of the Earth etc.). The proper magnetic environment has been traditionally obtained by making the measurements in magnetically shielded rooms (MSRs), which provide sufficient interference suppression for the SQUID-based measurements. However, typical commercial MSRs do not allow OPM-based neuromagnetic measurements since the sensitive operation of OPMs is limited to low-enough absolute magnetic fields; the magnetic field and its gradients in typical MSRs often exceed these limits. Thus, additional shielding to complement the passive MSR is needed.

The aim of this thesis is to create a proper magnetic environment for OPMs by

first surveying the remanent-field characteristics in the two MSRs of Aalto University and then enhancing these environments so that efficient neuromagnetic measurements with OPMs could be done. The thesis comprises three tasks: first, the magnetic fields inside the MSRs are measured and characterized. Second, based on these measurements, a coil set is designed and constructed to compensate for both static and dynamic magnetic fields. Third, the performance of the coil set is evaluated. Last, the thesis addresses the question whether the sensitive operation regime of OPMs can be achieved in these shielded rooms.

2 Background

This section provides an introduction to the subjects covered in this work. The generation of extracranial magnetic fields by the neural currents is first reviewed in a mathematical fashion. Also, the state-of-the-art instrumentation for recording these fields is covered. Then the physical principles of optically-pumped magnetometers are discussed together with the factors affecting their performance; design considerations for physical realizations of OPMs are also reviewed. Last, the principles of magnetic shielding are discussed.

2.1 Magnetoencephalography

MEG has established its role among neuroimaging methods due to its millisecond temporal resolution and decent spatial resolution. In addition to the use of MEG in fundamental neuroscience, it has also value in clinical work, where its most common use is in presurgical mapping of epileptic foci. The closest counterpart of MEG is electroencephalography (EEG), which has similar temporal resolution. The generators of the MEG and EEG signals are similar, though, the difference is that MEG measures the magnetic field while EEG measures the electric potential. These methods are mutually complementary, and it is often advantageous to measure both simultaneosly (see Ref. 11, for example). To some extent, the cost of MEG devices has hindered the adaptation of MEG among the neuroscientists and clinicians. Due to the lower cost of EEG, it remains the most widely used technique to record electric brain activity. To optimally capture the information in the extracranial electromagnetic fields by recording EEG and MEG simultaneously, it would thus be vital to bring down the cost of MEG by alternative methods for recording the extracerebral magnetic fields; optically-pumped magnetometers could provide such an alternative method.

2.1.1 Origins of the extracerebral fields

Brain collects, stores and processes information, maintains homeostasis, controls one's behaviour and enables consciousness and subjective experience. Human brain consists of about 100 billion neurons and ten times higher number of glial cells [12], making it the most complex organ in the human body. Neurons are the units that process information in the brain while it's generally thought that glial cells play only a supportive role: they insulate, support and nourish neighboring neurons [12]. However, the role of glial cells in information processing has also been speculated [12].

The neuron (or nerve cell) is confined by the cell membrane and consists of a soma, dendrites and an axon. The soma (or cell body) contains the cell nucleus and organelles. The dendrites are tree-like structures which extend from the soma and receive input from other neurons. Dendrites include synapses containing receptors, which allow information transfer between neurons. Axon is a projection of the neuron starting from the axon hillock at the soma and ending in the axon terminals. The

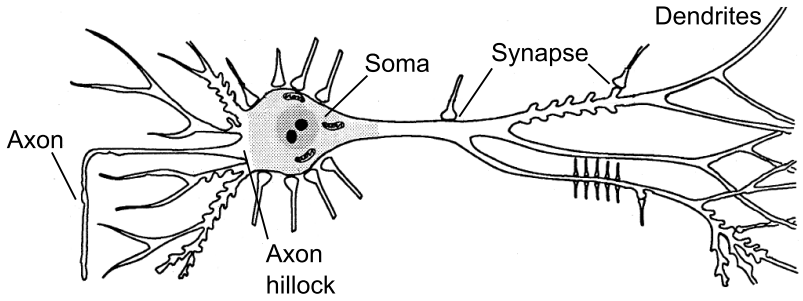

Figure 1: A pyramidal neuron. Figure is modified from Refs. 1 and 13.

axon carries information by electrical impulses (action potentials). A schematic drawing of a neuron is presented in Fig. 1.

Information is transferred in brain both chemically and electrically. Electrically, information is carried via action potentials which propagate along the axons until they reach the axon terminal, where they trigger a release of a neurotransmitter into the synaptic cleft (the gap between the pre- and postsynaptic neuron). Neurotransmitter molecules diffuse through the synaptic cleft and bind to the receptors of the postsynaptic cell, which in turn causes a change in the ionic permeability of the postsynaptic membrane and results in an ion flow through the membrane. This synaptic signalling carries information chemically. The synapses are either excitatory or inhibitory: current flow through an excitatory synapse depolarizes the cell (increases the membrane potential) while current flow through an inhibitory synapse hyperpolarizes the cell (decreases the potential).

These dendritic currents through the synapses eventually also affect the membrane potential at the axon hillock, which in turn determines whether the neuron fires an action potential or not: if the potential exceeds a certain threshold value, an action potential is fired. Typically, a neuron receives excitatory and inhibitory synaptic input from hundreds or thousands of other neurons while each synapse contributes to the potential at the axon hillock differently depending from various parameters, e.g., the distance of that synapse to the hillock. The net effect of all the synaptic currents at the axon hillock determines the potential and thereby also whether an action potential is fired.

Next, the different currents involved are listed and named and their contribution to the 'visible' MEG signals are inferred. First, the currents through the cell membrane at the synapses are called impressed currents. The currents flowing inside the cell are referred to as primary currents. The primary currents in turn involve return or volume currents flowing outside the cell since charge cannot accumulate; specifically, the volume currents will flow all around the conducting space and are driven by the electric field. Last, action potentials are travelling rapidly in the axons. When viewed sufficiently far away, the impressed and primary currents in dendrites have a dipolar morphology with field decaying as $1/r^2$. Correspondingly, the action potential can be thought to consist of two oppositely-directed current dipoles, thus forming a current quadrupole with field proportional to $1/r^3$. As the fields of these currents

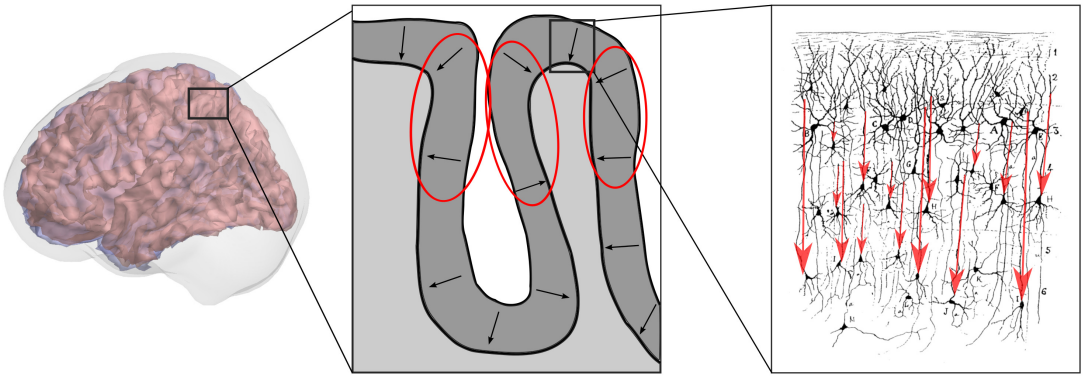

Figure 2: Sources of MEG signals. The intracellular postsynaptic currents of the apical dendrites of the pyramidal neurons are thought to be the main generators of the macroscopic extracranial fields (the red arrows on the rightmost panel). On a larger scale, these local currents sum to larger dipolar currents which lie in the gray matter and are oriented perpendicular to the surface of the cortex (middle panel). Examples of cortical areas whose sources generate the largest extracranial magnetic fields are highlighted with red ellipsoids. The panel on the right is based on a drawing by Ramón y Cajal in 1888.

in a single neuron are very small, spatial and temporal summation are needed to produce a macroscopically detectable magnetic field. The action potential propagates relatively fast and thus the temporal summation of the action potentials travelling in different axons is not very probable. In combination with the quicker field-decay, one can conclude that the probability of action potentials to generate macroscopic magnetic fields is not large. In contrast, the postsynaptic currents last longer to allow for temporal summation. Both impressed and primary currents are approximately current dipoles but the dipole moment of the impressed current is smaller due to the shorter length. Further, the impressed-current dipoles are scattered approximately uniformly on the membranes of the cylindrical dendrites leading to partial cancellation of the fields. Thus the fields generated by the impressed currents are not probably large, and the primary currents, i.e., the intracellular currents are the only currents that can explain the extracranial fields.

Cortex has favourable geometries which allow adequate spatial summation of the primary currents, namely the apical-dendrite bundles of the cortical pyramidal neurons (see Fig. 2). Therefore, the most probable generators of MEG signals are the intracellular currents flowing in the apical dendrites of the cortical pyramidal neurons. It has been estimated that about 10 000–50 000 synchronously active cells can generate large-enough extracranial magnetic fields [14].

There are few other noteworthy factors affecting the signal strength besides the strength and extent of the activation, namely, the depth and orientation of the primary current. Obviously, the larger the distance of the source to the sensors, the weaker the signal in general. The role of source orientation is not that apparent since the volume currents driven by the primary currents generate also a magnetic field,

which depends on the conductivity profile of the head. However, it can be shown that in a homogeneous spherical conductor radial primary currents do not produce any magnetic field outside the conductor since the field due to volume currents cancels the field of the primary current [1]. From this result one may 'extrapolate' that in head-shaped volume conductors the fields of radial sources are probably relatively small. Due to the orientation of the apical dendrities, the primary currents are oriented parallel to the surface normal of the cortex. Taking into account the meandering structure of the cortex, it can be concluded that MEG is much less sensitive to (radial) sources at the top of gyri than to the (tangential) sources in the fissures (see Fig. 2). Moreover, taking into account the trade-off in sensitivity between source orientation and depth, the sources with highest signals are most probably close to the superficial edges of the sulci.

2.1.2 Computation of neuromagnetic fields

General equations In this section, I describe both the physical and computational principles of electromagnetic field calculation in bioelectromagnetism. As usual in all electromagnetic field computations, the starting point is the Maxwell's equations

$$\nabla \cdot \mathbf{E} = \rho/\epsilon_0 \tag{1a}$$
$$\nabla \cdot \mathbf{B} = 0 \tag{1b}$$
$$\nabla \times \mathbf{E} = -\frac{\partial \mathbf{B}}{\partial t} \tag{1c}$$
$$\nabla \times \mathbf{B} = \mu_0 \mathbf{J} + \mu_0 \epsilon_0 \frac{\partial \mathbf{E}}{\partial t}, \tag{1d}$$

where $\mathbf{E}$ and $\mathbf{B}$ are the electric and magnetic fields, respectively, ρ and $\mathbf{J}$ are the total charge and current densities, respectively, $\epsilon_0 \approx 8.85 \times 10^{-12}$ F/m and $\mu_0 = 4\pi \times 10^{-7}$ Vs/Am are the permittivity and permeability of free space, respectively. A common practice in biomagnetic field computation is to use quasi-static approximation of the Maxwell's equations in which the propagative, inductive and capacitive effects are ignored and the Maxwell's equations reduce to the static form [1]. This approximation is called quasi-static because sources can be time-dependent even though other time-dependent effects are omitted. Usually the justification of this approximation is argumented by using the fact that with biological frequencies ($\leq$ 100 Hz) and tissue parameters, the wavelength of an electromagnetic wave is much larger than the spatial scale of the problem. However, one can question the validity of this approximation; see Ref. 15 and the discussion therein. Nevertheless, the quasi-static Maxwell's equations are:

$$\nabla \cdot \mathbf{E} = \rho/\epsilon_0 \tag{2a}$$
$$\nabla \cdot \mathbf{B} = 0 \tag{2b}$$
$$\nabla \times \mathbf{E} = 0 \tag{2c}$$
$$\nabla \times \mathbf{B} = \mu_0 \mathbf{J}. \tag{2d}$$

Since the curl of electric field vanishes (Eq. (2c)), it can be expressed as a gradient of scalar potential: $\mathbf{E} = -\nabla\phi$.

Next, the total current density is divided into two components: primary current density $\mathbf{J}_\mathrm{p}$ and volume (return) current density $\mathbf{J}_\mathrm{V}$. Primary current is related to the neuronal activity and can interpreted as a source of the signal while (ohmic) volume current is driven by the electric field $\mathbf{J}_\mathrm{V} = \sigma\mathbf{E} = -\sigma\nabla\phi$, where $\sigma = \sigma(\mathbf{r})$ is the conductivity. Thereby

$$\mathbf{J} = \mathbf{J}_\mathrm{p} + \mathbf{J}_\mathrm{V} = \mathbf{J}_\mathrm{p} - \sigma\nabla\phi. \tag{3}$$

Furthermore, primary currents are often modelled as ideal dipoles: [1]

$$\mathbf{J}_\mathrm{p}(\mathbf{r}) = \mathbf{Q}\delta(\mathbf{r} - \mathbf{r}_Q), \tag{4}$$

where $\mathbf{Q}$ is dipole moment, $\mathbf{r}_Q$ is the location of the source and $\delta(\mathbf{r})$ is the Dirac delta function:

$$\delta(\mathbf{r} - \mathbf{r}_Q) = \begin{cases} \infty, & \mathbf{r} = \mathbf{r}_Q \\ 0, & \mathbf{r} \neq \mathbf{r}_Q. \end{cases} \tag{5}$$

Taking divergence of the Eq. (2d) and using the vector identity $\nabla \cdot \nabla \times \mathbf{B} = 0$, one gets $\nabla \cdot \mathbf{J} = 0$ and hence magnetic field can be calculated from the Biot-Savart law. Furthermore, by taking divergence of Eq. (3), one arrives to Poisson equation for ϕ. Overall, the potential and the magnetic field of primary current can then be computed from the following equations

$$\nabla \cdot (\sigma\nabla\phi) = \nabla \cdot \mathbf{J}_\mathrm{p} \tag{6}$$

$$\mathbf{B}(\mathbf{r}) = \frac{\mu_0}{4\pi} \int \frac{[\mathbf{J}_\mathrm{p}(\mathbf{r}') - \sigma(\mathbf{r}')\nabla\phi(\mathbf{r}')] \times (\mathbf{r} - \mathbf{r}')}{|\mathbf{r} - \mathbf{r}'|^3} dV'. \tag{7}$$

The magnetic field is obtained by first solving potential from Eq. (6) and then calculating the integral in Eq. (7).

Piecewise homogeneous conductor Next, Eqs. (6) and (7) are considered in a piecewise homogeneous volume conductor. This is highly relevant geometry in biomagnetism, since the head conductivity can be approximated by three homogenous compartments: brain, skull and scalp. Explicitly, a piecewise homogeneous conductor with K surfaces S^k, $k = 1, ..., K$ separating the compartments has a primary current distribution $\mathbf{J}_\mathrm{p}$ embedded inside. Further, the conductivites inside and outside of surface k are denoted by σ_-^k and σ_+^k. By using boundary conditions for the potential and Green's theorem, Eq. (6) can be manipulated in this geometry to obtain a surface integral equation for the potential [16, 17]

$$\phi(\mathbf{r}) = \frac{2\sigma_s}{\sigma_-^l + \sigma_+^l}\phi_\infty(\mathbf{r}) - \frac{1}{2\pi}\sum_{k=1}^{K} \frac{\sigma_-^k - \sigma_+^k}{\sigma_-^l + \sigma_+^l} \int_{S^k} \phi(\mathbf{r}') \frac{(\mathbf{r} - \mathbf{r}')}{|\mathbf{r} - \mathbf{r}'|^3} \cdot \mathbf{dS}', \ \mathbf{r} \in S^l, \tag{8}$$

where $\phi_\infty(\mathbf{r})$ is the potential due to $\mathbf{J}_\mathrm{p}$ in an infinite homogeneous medium with conductivity σ_s (interpreted as a unit conductivity):

$$\phi_\infty(\mathbf{r}) = \frac{1}{4\pi\sigma_s} \int_V \frac{\mathbf{J}_\mathrm{p}(\mathbf{r}') \cdot (\mathbf{r} - \mathbf{r}')}{|\mathbf{r} - \mathbf{r}'|^3} dV'. \tag{9}$$

A similar equation can be also obtained for the magnetic field [18]

$$\mathbf{B}(\mathbf{r}) = \mathbf{B}_\infty(\mathbf{r}) - \frac{\mu_0}{4\pi}\sum_{k=1}^{K}(\sigma_-^k - \sigma_+^k)\int_{S^k}\phi(\mathbf{r}')\mathbf{dS}' \times \frac{(\mathbf{r}-\mathbf{r}')}{|\mathbf{r}-\mathbf{r}'|^3}, \tag{10}$$

where $\mathbf{B}_\infty(\mathbf{r})$ is the magnetic field due to a primary current distribution in an infinite, vacuum-like medium:

$$\mathbf{B}_\infty(\mathbf{r}) = \frac{\mu_0}{4\pi}\int_V \frac{\mathbf{J}_\mathrm{p}(\mathbf{r}')\times(\mathbf{r}-\mathbf{r}')}{|\mathbf{r}-\mathbf{r}'|^3}dV'. \tag{11}$$

Boundary element method To solve the potential and magnetic field from Eqs. (8) and (10) in arbitrarily-shaped piecewise homogeneous conductors, numerical and computational methods are needed. Since the equations are cast in surface integral form, a convenient choice is boundary element method (BEM). Here, the idea behind boundary element method is shown by introducing the process which yields the BEM solutions for potential and magnetic field using constant basis functions and collocation weighting. The text and notations follow those in Ref. 17.

First, each surface S^l is discretized into n^l nodes and t^l triangular elements T_i^l. Then the following notations are defined to make the expressions simpler

$$\phi^l = \phi(\mathbf{r}),\ \mathbf{r}\in S^l \tag{12}$$

$$b^l = \frac{2\sigma_s}{\sigma_-^l+\sigma_+^l}\phi_\infty(\mathbf{r}),\ \mathbf{r}\in S^l \tag{13}$$

$$c^{lk} = 2\frac{\sigma_-^k-\sigma_+^k}{\sigma_-^l+\sigma_+^l} \tag{14}$$

$$D^{lk}[g](\mathbf{r}) = \frac{1}{4\pi}\int_{S^k} g(\mathbf{r}')\frac{(\mathbf{r}-\mathbf{r}')}{|\mathbf{r}-\mathbf{r}'|^3}\cdot\mathbf{dS}',\ \mathbf{r}\in S^l, \tag{15}$$

where $D^{lk}[g]$ is called the double-layer integral operator in bioelectromagnetism. Eq. (8) then translates into

$$\phi^l = b^l - \sum_{k=1}^{K} c^{lk}D^{lk}[\phi^k]. \tag{16}$$

Next, the solution ϕ^l is approximated as a linear combination of N^l basis functions χ_i with coefficients ξ_i

$$\phi^l \approx \sum_{i=1}^{N^l}\xi_i^l\chi_i^l \tag{17}$$

and it is inserted to Eq. (16) to get

$$\sum_{i=1}^{N^l}\xi_i^l\chi_i^l = b^l - \sum_{k=1}^{K}c^{lk}\sum_{m=1}^{N^k}\xi_m^k D^{lk}[\chi_m^k]. \tag{18}$$

The error of the solution is minimized by taking the inner product of the residual and weight functions w_j^l over the solution domain; effectively, this means multiplying

Eq. (18) with weight function and integrating it over S^l:

$$\sum_{i=1}^{N^l} \xi_i^l \int_{S^l} w_j^l \chi_i^l dS = \int_{S^l} w_j^l b^l dS - \sum_{k=1}^{K} c^{lk} \sum_{m=1}^{N^k} \xi_m^k \int_{S^l} w_j^l D^{lk}[\chi_m^k] dS. \tag{19}$$

Now that Eq. (19) has been derived, the basis and weight functions have to be chosen. Different BEM solvers differ by the choice of these functions; for example, in linear Galerkin BEM, the weight and basis functions are both chosen to be linear. Here, the the matrix equations are derived in the simplest case of constant basis functions and collocation weighting:

$$\chi_i^l(\mathbf{r}) = \begin{cases} 1, & \text{if } \mathbf{r} \in T_i^l \\ 0, & \text{if } \mathbf{r} \notin T_i^l \end{cases} \tag{20}$$

$$w_j^l = \delta(\mathbf{r} - \mathbf{c}_j^l), \tag{21}$$

where c_j^l is the centroid of the jth triangle on surface l. Substituting these into Eq. (19) yields [17]

$$\xi_j^l = b_j^l - \sum_{k=1}^{K} c^{lk} \sum_{m=1}^{t^k} \xi_m^k \Omega_{jm}^{lk}, \tag{22}$$

where Ω_{jm}^{lk} is the normalized solid angle spanned by T_m^k at $\mathbf{c}_j^l$:

$$\Omega_{jm}^{lk} = \frac{1}{4\pi} \int_{T_m^k} \frac{(\mathbf{c}_j^l - \mathbf{r}')}{|\mathbf{c}_j^l - \mathbf{r}'|^3} \cdot \mathbf{dS}'. \tag{23}$$

The above can be cast to a simple matrix form:

$$\boldsymbol{\xi}^l = \mathbf{b}^l - \sum_{k=1}^{K} c^{lk} \boldsymbol{\Omega}^{lk} \boldsymbol{\xi}^k, \tag{24}$$

where the dimensions of $\boldsymbol{\xi}^l$ and $\mathbf{b}^l$ are $t^l \times 1$ while the dimensions of $\boldsymbol{\xi}^k$ and $\boldsymbol{\Omega}^{lk}$ are $t^k \times 1$ and $t^l \times t^k$, respectively. By collecting the terms from all the equations for different surfaces, one finally gets [17]

$$\begin{pmatrix} \boldsymbol{\xi}^1 \\ \boldsymbol{\xi}^2 \\ \vdots \\ \boldsymbol{\xi}^K \end{pmatrix} = \begin{pmatrix} \mathbf{b}^1 \\ \mathbf{b}^2 \\ \vdots \\ \mathbf{b}^K \end{pmatrix} - \begin{pmatrix} c^{11}\boldsymbol{\Omega}^{11} & c^{12}\boldsymbol{\Omega}^{12} & \cdots & c^{1K}\boldsymbol{\Omega}^{1K} \\ c^{21}\boldsymbol{\Omega}^{21} & c^{22}\boldsymbol{\Omega}^{22} & \cdots & c^{2K}\boldsymbol{\Omega}^{2K} \\ \vdots & \vdots & \ddots & \vdots \\ c^{K1}\boldsymbol{\Omega}^{K1} & c^{K2}\boldsymbol{\Omega}^{K2} & \cdots & c^{KK}\boldsymbol{\Omega}^{KK} \end{pmatrix} \begin{pmatrix} \boldsymbol{\xi}^1 \\ \boldsymbol{\xi}^2 \\ \vdots \\ \boldsymbol{\xi}^K \end{pmatrix} \tag{25}$$

$$\Leftrightarrow \boldsymbol{\xi} = \mathbf{b} - \tilde{\boldsymbol{\Omega}}\boldsymbol{\xi}, \tag{26}$$

from which the coefficients can be solved to obtain the BEM solution for the potential:

$$\boldsymbol{\xi} = (\mathbf{I} + \tilde{\boldsymbol{\Omega}})^{\dagger}\mathbf{b}, \tag{27}$$

where $\mathbf{I}$ is the identity matrix with same dimensions as $\tilde{\boldsymbol{\Omega}}$ and $\dagger$ denotes pseudoinverse.

After the constant collocation BEM solution for the potential has been obtained, magnetic field can be calculated from Eq. (10), which can be modified into

$$\mathbf{B}(\mathbf{r}) = \mathbf{B}_\infty(\mathbf{r}) + \sum_{k=1}^{K} d^k \mathbf{D}_\mathbf{B}^k \boldsymbol{\xi}^k, \tag{28}$$

where $d^k = \frac{\mu_0}{4\pi}(\sigma_+^k - \sigma_-^k)$ and the elements of $\mathbf{D}_\mathbf{B}^k \in \mathbb{R}^{3\times t^k}$ are given by

$$\mathbf{D}_{\mathbf{B}_i}^k(\mathbf{r}) = \int_{T_i^k} \mathbf{dS}' \times \frac{(\mathbf{r}-\mathbf{r}')}{|\mathbf{r}-\mathbf{r}'|^3}. \tag{29}$$

However, in practice the above formulation is not fully sufficient since numerical inaccuracies can arise due to the high contrast between the conductivities of skull and brain/scalp. To tackle this problem, the so-called isolated source approach (ISA) has been developed. I do not discuss ISA here, but the method is introduced and discussed in Refs. 19 and 20.

2.1.3 Conventional instrumentation

In this section, I will shortly review the instrumentation of the state-of-the-art MEG systems. Typical range of neuromagnetic fields is 50–500 fT [1] while the Earth's geomagnetic field is of order of tens of μT thus neuromagnetic signals are about 10^9 times smaller than the geomagnetic field. Due to the weakness of these fields very sensitive magnetic field sensors and sophisticated magnetic noise cancellation methods are needed in the MEG systems.

A typical MEG set-up consists of the following components:

- Magnetically shielded room
- Superconducting Quantum Interference Devices (SQUIDs)
- Dewar and cryogenics
- Gantry (the mechanical system supporting the Dewar)
- Electronics.

The MEG device is operated in a magnetically shielded room to reduce the perturbations caused by external AC and DC fields such as the fields of moving vehicles and elevators. Currently, the only sensors with an adequate sensitivity to enable practical whole-scalp magnetic field mappings of the brain are SQUIDs. SQUIDs are based on superconductivity and quantum physics; basically, SQUID is a superconductive ring interrupted with one or two Josephson junctions [21]. Using appropriate feedback electronics, one can deduce the magnetic flux and hence the magnetic field from the measured voltage across the SQUID. However, because of their small size, SQUIDs alone do not efficiently measure neuromagnetic signals. Therefore, they are usually coupled with flux transformers which collect magnetic flux from a larger area and direct it to the SQUID. The flux transformer can be configured in different geometries

to enable measurements of the different components of the field or field gradients. For example, the state-of-the-art MEG system of Elekta Oy (Helsinki, Finland) contains 306 channels assembled in triplets at 102 locations covering whole scalp. Each triplet consists of one magnetometer measuring the normal component of the field with respect to the subject's head and two planar gradiometers which measure the tangential gradients of the normal field component.

The temperature of SQUIDs has to be maintained below the critical level, which is obtained by immersing them in liquid helium ($T = 4.2$ K) in a nonmagnetic Dewar. The bulky and heavy Dewar needs a mechanical support system, Gantry. The electronics of MEG system provide the negative feedback to the SQUIDs and perform other signal processing tasks such as filtering, but they also drive the head-position tracking coils and monitor the liquid helium level [2].

2.2 Optical magnetometry

In optical magnetometry, magnetic field is measured by utilizing interactions between resonant light and a sample. In optically-pumped magnetometers, the magnetization of a sample (typically alkali vapor) is detected by measuring transmission or polarization rotation of a light beam. Next, the principles of optical magnetometry are reviewed.

2.2.1 Operating principle

The optical measurement scheme can be divided into three main parts: polarization of alkali atoms by means of optical pumping, temporal evolution of the polarization in the applied magnetic field, and an optical measurement of the polarization state. A typical setup for an optical measurement of magnetic field is illustrated Fig. 3. In this scheme, a circularly-polarized pump light beam travelling to positive x-direction orients the spins of the alkali atoms in the vapor cell to the direction of the beam. In the presence of a magnetic field, these spins undergo Larmor precession around the magnetic field. This precession in turn alters the absorptive and dispersive properties of the alkali atoms; these alterations can be detected by measuring either the transmission or polarization rotation of a linearly-polarized probe beam. In the presented scheme, the probe beam is chosen to be orthogonal to the pump beam; however, this does not have to be the case as optically-pumped magnetometers operating with a single laser with elliptic polarization have been demonstrated [22] and a single circularly-polarized beam can be used to both pump and probe if absorption is measured instead of the polarization rotation [23]; for more about sensor desing, see Sec. 2.2.3. Next, the physics of optical magnetometers is introduced based on the first chapter of Ref. 4.

Optical pumping refers to a process where light is used to redistribute atoms in their energy levels. Here, the optical pumping process is demonstrated through a simple example (for a comprehensive review of optical pumping, see Ref. 24). Suppose that we have atoms with an energy level diagram shown in Fig. 4 and that initially $\mathbf{B} = 0$. The atoms are illuminated by a circularly-polarized light beam propagating to the positive x-direction (as in Fig. 3). The atoms in the ground-state sublevel $-\frac{1}{2}$ (denoted as $|-\rangle_x$) can absorb a photon and jump to an excited-state sublevel $+\frac{1}{2}$ while the atoms in the ground-state sublevel $+\frac{1}{2}$ ($|+\rangle_x$) cannot due to angular momentum selection rules. The excited-state sublevel $+\frac{1}{2}$ is not stable: this state decays quickly and the atom falls back to either of the ground-state sublevels. The probability to decay to the ground-state sublevel $+\frac{1}{2}$ is, however, higher and thus, if no relaxation processes exist, all the atoms will eventually be pumped to the ground-state sublevel $+\frac{1}{2}$, which does not react to light and is thereby a dark state; correspondingly $|-\rangle_x$ is a bright state. The preceding simple example illustrates how pumping occurs through two different mechanisms: depopulation pumping and repopulation pumping [24]. In depopulation pumping, the frequency of the light is set to excite a certain hyperfine ground state while the repopulation pumping occurs when the excited state decays spontaneously.

Now magnetic field $\mathbf{B} = B\,\hat{\mathbf{e}}_\mathbf{z}$ is switched on. In the magnetic field, the energies

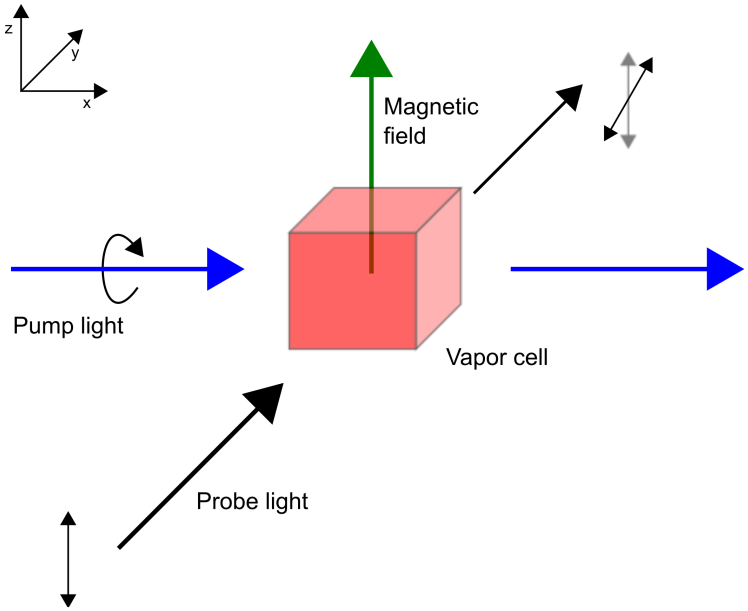

Figure 3: A schematic of a typical setup for an optical measurement of magnetic field. A circularly-polarized pump light polarizes the alkali atoms in the vapor cell creating a net magnetic moment to the x-direction. The magnetic moments (spins) undergo Larmor precession in the presence of magnetic field. The state of the magnetic moment is detected by measuring either transmission or polarization rotation of a linearly-polarized probe light.

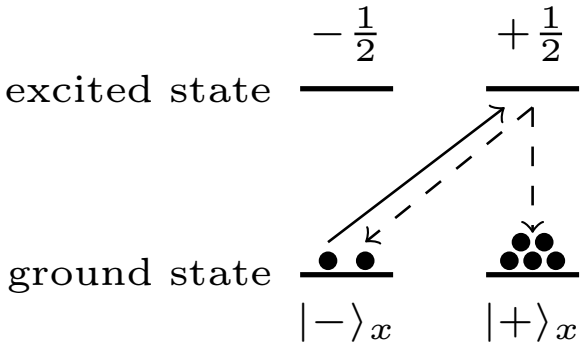

Figure 4: A simple example of an optical pumping scheme. Atoms in the ground-state sublevel –1/2 are excited to the excited-state sublevel +1/2 (solid arrow). The excited state then decays spontaneously to either of the ground state sublevels (dashed arrows).

of the ground-state sublevels are shifted as follows: energy of $|-\rangle_x$ is shifted by $-\hbar\Omega_L/2$ and energy of $|+\rangle_x$ by $\hbar\Omega_L/2$, where $\hbar = 1.055 \times 10^{-34}$ Js is the reduced Planck constant, and Ω_L is Larmor frequency, which is directly propotional to the magnetic field: $\Omega_L = \gamma B$; the constant γ is gyromagnetic ratio of the atom species.

Since the magnetic field is oriented to z-direction, it is convenient to choose the quantization axis along z-direction and expand the ground states as [4]

$$|+\rangle_x = \frac{|-\rangle_z + |+\rangle_z}{\sqrt{2}} \tag{30}$$

$$|-\rangle_x = \frac{|-\rangle_z - |+\rangle_z}{\sqrt{2}}. \tag{31}$$

Assuming that magnetic field is turned on at $t = 0$ and ignoring light–atom interactions, the time-development of the state of the atomic ensemble $|\psi(t)\rangle$ is given by

$$|\psi(t)\rangle = \sqrt{\frac{1}{2}}\left(e^{i\Omega_L t/2}|-\rangle_z + e^{-i\Omega_L t/2}|+\rangle_z\right). \tag{32}$$

The probability of finding the atom at the bright state is thereby:

$$P = |\langle\psi(t)|-\rangle_x|^2 = \sin^2(\Omega_L t/2). \tag{33}$$

This probability oscillates sinusoidally at a Larmor frequency. This sinusoidal modulation is nothing more than the well-known Larmor precession: the precession of spins about an external magnetic field. Since the state is bright, the light–atom interaction is modulated correspondingly and thereby the probe light carries information about the Larmor frequency and thus also about the magnetic field.

The previous treatment concisely illustrates the phenomena behind optical magnetometry; however, numerous simplifications were made, especially spin relaxation mechanisms were completely neglected. For a more rigorous analysis, the treatment must be cast to a density-matrix formalism. Density matrix allows describing a quantum system in a mixed state, which is a statistical ensemble of many quantum states. Considering an ensemble of atoms whose states can be expanded to orthonormal basis as [4]

$$|\psi_i\rangle = \sum_m |m\rangle\langle m|\psi_i\rangle, \tag{34}$$

the matrix elements of the density matrix are given by [4]

$$\rho_{m,n} = \sum_i \langle m|\psi_i\rangle\langle\psi_i|n\rangle. \tag{35}$$

Using the density matrix, expectation value of observable A can be calculated as $\langle A\rangle = \mathrm{Tr}(\rho A)$. Time evolution of the density matrix is the dictated by Liouville-von Neumann equation

$$\frac{\partial\rho}{\partial t} = -\frac{i}{\hbar}[H, \rho], \tag{36}$$

where H is the Hamiltonian and brackets denote a commutator.

The density-matrix equation describing the optical magnetometer scheme can be obtained from Eq. (36) with the corresponding Hamiltonian and by adding additional terms describing collisions between the atoms; the equation is then [4, 25, 26]

$$\frac{d\rho}{dt} = A_{hf}\frac{[\mathbf{I}\cdot\mathbf{S},\rho]}{i\hbar} + \mu_B g_S \frac{[\mathbf{B}\cdot\mathbf{S},\rho]}{i\hbar} + \frac{\varphi(1+4\langle\mathbf{S}\rangle\cdot\mathbf{S})-\rho}{T_{SE}} + \frac{\varphi-\rho}{T_{SD}} + R[\varphi(1+2\mathbf{s}\cdot\mathbf{S})-\rho] + D\nabla^2\rho, \tag{37}$$

where $\mathbf{S}$ is the electron spin, $\mathbf{I}$ is the nuclear spin, $\varphi = \rho/4 + \mathbf{S}\cdot\rho\mathbf{S}$ is the nuclear part of the density matrix, A_{hf} is the hyperfine constant of the magnetic-dipole coupling, $g_S \approx 2.002$ is the electron g-factor, $\mu_B \approx 9.274\times10^{-24}$ J/T is the Bohr magneton, R is the optical pumping rate, T_{SD} is the spin-destruction relaxation time, T_{SE} is the spin-exchange collision time, D is the diffusion coefficient and $\mathbf{s}$ is the optical-pumping vector, which defines the direction and degree of polarization of the laser beam; for a circularly-polarized pump beam $|\mathbf{s}| = 1$.

The first two terms on the right-hand side of Eq. (37) come from the hyperfine and magnetic interaction Hamiltonians. The third and fourth terms describe the spin relaxation mechanisms, namely, spin-exchange and spin-destruction collisions between the atoms. These relaxation mechanisms and how they affect the sensitivity of the optical magnetometer are discussed in more detail in Sec. 2.2.2. The fifth and sixth terms are optical pumping and diffusion terms.

In the so-called spin-exchange-relaxation-free (SERF) setup, where the spin-exchange collisions do not contribute to the spin relaxation (see Sec. 2.2.2 for a more detailed discussion of the SERF limit), Eq. (37) can be simplified to the Bloch equation [4]

$$\frac{d\mathbf{S}}{dt} = \frac{1}{q}\left[\gamma^e\mathbf{B}\times\mathbf{S} + R_{\mathrm{OP}}\left(\frac{1}{2}s\hat{\mathbf{e}}_{\mathbf{x}} - \mathbf{S}\right) - R_{\mathrm{rel}}\mathbf{S}\right], \tag{38}$$

where q is the nuclear slowing-down factor, $\gamma^e \approx 2\pi\times 28025$ MHz/T is the gyromagnetic ratio of an electron, R_{OP} is the optical pumping rate, $s = 1$ is the length of the optical pumping vector, and R_{rel} is the spin relaxation rate in the absence of optical pumping. The quasi-steady-state solution to Eq. (38) can be found by assuming slowly changing magnetic fields and is given by [4, 27]

$$S_y = S_0\frac{\beta_z - \beta_x\beta_y}{1+(\beta_x^2+\beta_y^2+\beta_z^2)}, \tag{39}$$

where $S_0 = R_{\mathrm{OP}}/[2(R_{\mathrm{OP}}+R_{\mathrm{rel}})]$ is the equilibrium spin polarization and β_i is introduced as a dimensionless magnetic field parameter:

$$\beta_i = \frac{\gamma^e B_i}{R_{\mathrm{OP}}+R_{\mathrm{rel}}}. \tag{40}$$

Since we are effectively measuring the projection of the spin to the y-direction, Eq. (39) gives the magnetometer signal.

Certain interesting inferences can be made from Eq. (39). First, if the magnetic field is small enough, i.e. $\sqrt{\beta_x^2+\beta_y^2+\beta_z^2} \ll 1$, one can approximate $S_y \approx S_0\beta_z$

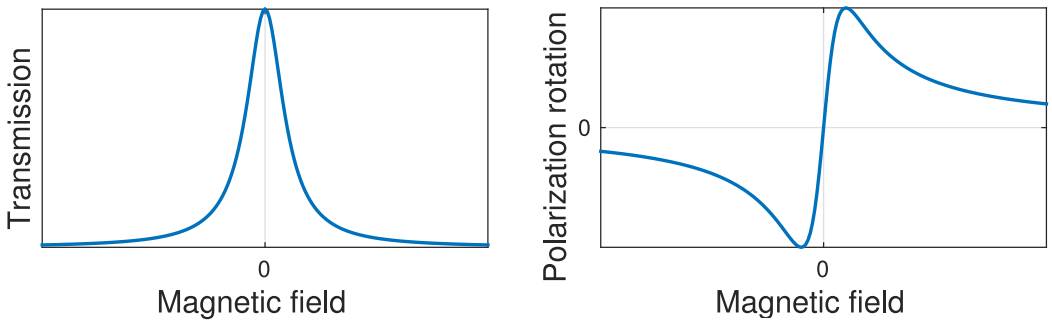

Figure 5: Characteristic shapes of the optically-pumped magnetometer signals as a function of magnetic field. Please note that the presented transmission signal is obtained when the pump and probe beams are in parallel.

and see that the magnetometer is most sensitive to the magnetic field component perpendicular to the pump and probe beams. Second, one can infer from it how to measure the different magnetic field components by using modulation [27]. Supposing that the magnetic field along the x and y axes is modulated so that the field is a sum of the original field β^0 and modulation field:

$$\beta_x = \beta_x^0 + \beta_x^{\mathrm{mod}} \sin(\omega_x t) \tag{41}$$

$$\beta_y = \beta_y^0 + \beta_y^{\mathrm{mod}} \sin(\omega_y t) \tag{42}$$

and assuming that the magnetic field and its modulation amplitudes are small enough ($\sqrt{\beta_x^2 + \beta_y^2 + \beta_z^2} \ll 1$), Eq. (39) can expanded as follows [27]

$$S_y \approx S_0[\beta_z - \beta_x^0\beta_y^0 - \beta_x^0\beta_y^{\mathrm{mod}} \sin(\omega_y t) - \beta_y^0\beta_x^{\mathrm{mod}} \sin(\omega_x t)]. \tag{43}$$

Thus, the x- and y-components of the magnetic field can be deduced from the measured signal by using lock-in detection. It should be emphasized that the modulation of the y-component of the magnetic field gives x-component and vice versa.

The characteristic shapes of the transmission and polarization rotation signals as a function of magnetic field are shown in Fig. 5. The transmission signal in this figure is obtained the when pump and probe beams are in parallel; it thus differs from the setup presented in Fig. 3. The transmission signal has a shape of Lorentzian and is centered at zero magnetic field. In the zero field, the majority of the spins are oriented parallel to the probe beam due to pumping and the transmission reaches its maximum. While in non-zero field, the spins undergo Larmor precession which causes their net orientation to differ from the probe beam direction; thereby the transmission decreases.

2.2.2 Sensitivity and noise

The main sources of noise in optically-pumped magnetometers include photon shot noise, quantum projection noise of the spin measurement and technical noise such as laser intensity noise and thermal noise from magnetic shielding. The photon

shot noise arises from the fact that the illuminating light consists of single particles (photons), while the spin-projection noise originates from the uncertainty in the spin measurement, which is governed by the Heisenberg's principle. When an optical magnetometer is designed optimally, the spin-projection noise dominates over the photon shot noise [28, 29] and thus sets the fundamental limit to the sensitivity of the optically-pumped magnetometer [3, 28]:

$$\delta B = \frac{1}{\gamma}\frac{1}{\sqrt{N\tau T_{\mathrm{rel}}}}, \tag{44}$$

where γ is the gyromagnetic ratio of the atoms, N is the number of atoms, τ is the measurent time and T_{rel} is the relaxation time of the atoms. The conditions in which sensitivity is limited by Eq. (44) include short measurement time, i.e. $\tau < T_{\mathrm{rel}}/N$ [28], and that the probe is tuned sufficiently far from the resonance so that the medium is optically thin [29]; however one can also use Faraday rotation in an optically thick sample while ensuring that the back-action of the probe beam does not contribute to the spin measurement [4]. Eq. (44) shows that the sensitivity can be enhanced by increasing the number of atoms or by prolonging the relaxation time. By taking into account all the relaxation mechanisms, the total relaxation rate in Eq. (44) can be written as [4]

$$\frac{1}{T_{\mathrm{rel}}} = \frac{1}{T_{\mathrm{rel}}^{\mathrm{col}}} + \frac{1}{T_{\mathrm{rel}}^{\mathrm{bg}}} + \frac{1}{T_{\mathrm{rel}}^{\mathrm{w}}} + \frac{1}{T_{\mathrm{rel}}^{\mathrm{oth}}}, \tag{45}$$

where $T_{\mathrm{rel}}^{\mathrm{col}}$ is the relaxation time due to atom–atom collisions, $T_{\mathrm{rel}}^{\mathrm{bg}}$ is the relaxation time due to collisions of the alkali atoms to buffer gas atoms, $T_{\mathrm{rel}}^{\mathrm{w}}$ is the wall-induced relaxation time and $T_{\mathrm{rel}}^{\mathrm{oth}}$ is the relaxation time due to other mechanisms, which can be minimized with appropriate design choices. Next, these different relaxation mechanisms are reviewed and methods for minimizing them are introduced.

The main factors that contribute to the relaxation time are the collisions between the atoms and the collisions of the atoms to cell walls, which are especially harmful since they depolarize the atoms completely. To diminish the relaxation due to wall collisions, buffer gas is added to the cell and antirelaxation surface coatings of the cell are used. The addition of a buffer gas to the cell make atom–wall collisions less frequent by forcing the atoms to diffuse through the cell [4]. In turn, antirelaxation coating of the cell increases the number of wall-bounces an atom can undergo before complete depolarization; proper wall coatings can increase the number of bounces to thousands [30] or even to millions [31]. Compared to the buffer gas, antirelaxation cell coatings have certain advantages: suppression of gradient broadening, larger optical rotation signals and lower laser-power requirements [4]; however, surface coating is a rather laborous process and does not always yield reproducible results (for example, even small defects in coating can ruin its performance) [3].

There is an optimal buffer gas pressure, which minimizes the contribution of buffer gas and wall collisions to relaxation; in this pressure, the combined relaxation rate due to buffer gas and wall collisions is given by [4]

$$\frac{1}{T_{\mathrm{rel}}^{\mathrm{bg}}} + \frac{1}{T_{\mathrm{rel}}^{\mathrm{w}}} = 2\frac{\sqrt{D_0\gamma_0}}{\beta L}, \tag{46}$$

where D_0 is the diffusion constant, γ_0 is the relaxation rate induced by the buffer gas, β is a constant of order unity which depends on the cell geometry and $L \sim \sqrt[3]{V}$ is the characteristic size of the cell; both D_0 and γ_0 are at buffer gas density of 1 amagat[1].

The atoms also collide with each other in the vapor cell. These atom–atom collisions can be divided into two subtypes: spin-exchange and spin-destruction collisions, of which spin-exchange collisions dominate [3]. In spin-exchange process, the total spin is conserved but the orientation of electron spins of the atoms can change; this process may thereby lead to decoherence of spins. Correspondingly, in spin-destruction collisions, total spin is not conserved. The relaxation time due to atom–atom collisions can be approximated as [4]

$$T_{\mathrm{rel}}^{\mathrm{col}} = \frac{1}{n\sigma_{\mathrm{col}} v}, \tag{47}$$

where n is the vapor density, σ_{col} is the collision cross section and v is the average relative velocity of the atoms. Typically the cross section for spin-exchange collision is decades higher than that for spin-destruction collision; for example, for ^{87}Rb the spin-exchange cross section is $\sim 2 \times 10^{-14}$ cm^2 while the corresponding value for spin-destruction is $\sim 9 \times 10^{-18}$ cm^2 [23]. If we assume high atom density, then the relaxation time is dominated by atom–atom collisions and the sensitivity can be written as [4]

$$\delta B = \frac{1}{\gamma}\sqrt{\frac{v\sigma_{\mathrm{col}}}{V\tau}}, \tag{48}$$

where V is the volume of the cell.

In the SERF regime, the contribution of spin-exchange collisions to relaxation can be effectively tuned off and then the relaxation, and thereby also sensitivity, are dictated by the spin-destruction collisions with much smaller cross sections. Thus, according to Eq. (48), much higher sensitivities can be achieved in the SERF regime. The first realizations of such regime were made in Refs. 33 and 34, where it was observed that spin-exchange relaxation can be possibly suppressed by increasing the rate of spin-exchange collisions beyond the Larmor frequency. The conditions for SERF regime include sufficiently high atom density (cell temperature) and low magnetic field [4, 25]; in particular, magnetic field should not exceed about 10 nT [3].

As the spin state of the alkali atoms in optical magnetometers is detected via light transmission or polarization rotation of a linearly polarized light and the atoms are pumped by a laser beam, there are various contributions to the measurement noise from the use of light. If polarization rotation is measured, the photon-shot-noise-limited sensitivity of the measured optical rotation angle θ is [4]

$$\delta\theta \simeq \frac{1}{2\sqrt{\dot{N}_{\mathrm{ph}}\tau}}, \tag{49}$$

where $\dot{N}_{\mathrm{ph}}$ is the probe-photon flux (photons/s) after the sample. However, as mentioned above, when an optically-pumped magnetometer is employed optimally,

[1] An amagat is a unit of number density and it is defined as the number of ideal gas molecules per unit volume at 1 atm and 0°C [32].

the photon shot noise does not exceed the spin-projection noise. Also, laser-intensity fluctuations cause noise especially in the light transmission measurement but polarization rotation measurement is less sensitive to this source of noise. Furthermore, pump and probe beams can shift the energies of the Zeeman sublevels of the alkali atoms through the AC stark effect, and hence also the spin-precession frequency may change [4]. This in turn produces a fictitious magnetic field to the direction of the laser beam, which is proportional to the degree of circular polarization of the light [35]. There are various ways to eliminate the effect of AC stark shift on the measurement. For instance, one can choose the measurement geometry so that the fictitious magnetic field is perpendicular to the measured magnetic field [3] or one can tune the laser to a frequency at which the noise due to the AC stark shift crosses zero [36].

Other sources of noise include environmental noise, noise due to imperfectly polarized light, frequency-to-amplitude conversion noise and magnetic noise arising from Johnson–Nyquist thermal currents. One can suppress environmental noise by using a magnetically shielded room; however, in such rooms there is still a finite residual magnetic field due to imperfect shielding and the Johnson–Nyquist thermal currents and thermal fluctuations of magnetic domains in the innermost shielding layer. Typically, the magnetic DC fields are on the order of $\sim$100 nT while the gradients are $\sim$100 pT/cm in standard two-layer MSRs [9]. Therefore, to operate SERF OPMs in standard MSRs, additional magnetic field compensation is needed, since the SERF OPMs lose sensitivity in magnetic environment where fields exceed (depending on the sensor) about 10 nT as described earlier. The different methods to magnetic field shielding are discussed in detail in Sec. 2.3.

2.2.3 Sensor design

In this section, I will introduce the basic components of a physical realization of an optically-pumped magnetometer and discuss the alternative ways of building these sensors. This section will mostly consider optically-pumped-magnetometer designs most suitable for biomagnetic applications, namely, chip-scale optically-pumped magnetometers (CSOPMs) in SERF regime [37]. CSOPMs are particularly attractive for biomagnetic applications because of their small size; these sensors could be placed within few millimetres from the scalp and a dense whole-scalp MEG arrays could be constructed. The feasibility of such sensors to record biomagnetic signals has also been demonstrated (see Refs. 5, 6 and 8, for example).

The main components of an optically-pumped magnetometer are light source(s), a vapor cell, optics, vapor cell heaters, and photodetectors. Light sources provide the pumping and probing beams while photodetectors (such as photodiodes) are used to detect amplitude or polarization of the transmitted light. An optionally antirelaxation-coated vapor cell contains the alkali atoms together with buffer and quenching gases. The vapor cell is heated to obtain sufficiently high atomic density necessary for the SERF regime. Optics are used to direct and polarize the light beams.

Optically-pumped magnetometer can generally be build in two different ways

depending on the application: either as a stand-alone, fully integrated magnetic sensor or as a sensor head fibre-optically coupled to a central control unit [4]. Each of the constructions have their own advantages. Fully integrated sensors enable inexpensive individual fabrication while the fibre-optically coupled sensors heads can be all interrogated with the same laser, which is particularly beneficial for large sensor arrays. In addition, the laser and electronics can cause magnetic noise when in the vicinity of the detection volume so this noise can be reduced in the fibre-optically coupled sensor heads where the laser is well-separated from the vapor cell. In addition, in the fibre-optical sensors, a higher-intensity laser with better noise characteristics can be used [4].

The best sensitivity is obtained by using two separate lasers, but high sensitivity can be also achieved with only one [4]. The main advantages of single-laser setups include convenience and reduced price. As noted before, one way to construct a single-laser optically-pumped magnetometer is to use elliptical polarization of the beam as a compromise between circular pumping and linear probing beams [22]. In this scheme, the spins have to be tilted with a relatively strong modulated magnetic field to obtain a signal from the magnetometer. The modulation broadens the magnetic resonance but at the same time decreased $1/f$ and optical noise and consequently lead to high sensitivity. The single-laser scheme can be also obtained by measuring light absorption instead of Faraday rotation [23]. However, it is usually more advantageous to measure the Faraday rotation since it is less sensitive to laser-intensity noise and can tolerate much higher optical thickness of the vapor due to detuning of the light from the optical resonance [38].

The vapor cells for CSOPMs are usually fabricated using microelectromechanical systems (MEMS) techniques [39] due to their small size (sidelength of the cell is few millimetres). The cell is filled with the alkali atom gas (such as rubidium) and buffer gas which slows the diffusion of the atoms (see Sec. 2.2.2 for discussion about the role of the buffer gas). The most common buffer gases include nitrogen, neon, argon, helium, hydrogen and xenon [4]. Specific care should be taken when choosing the material of the vapor cell; it must be nonmagnetic and should have minimal magnetic noise arising from the thermal motion of the charge carriers. This is especially important in CSOPMs since the cell walls are close to the sensitive volume. It has been estimated that by growing the silicon of the vapor cell appropriately, the magnetic field noise arising from cell body can be reduced from few $\mathrm{fT}/\sqrt{\mathrm{Hz}}$ to strictly below 1 $\mathrm{fT}/\sqrt{\mathrm{Hz}}$ [40]. Interestingly, the authors also showed that the presence of alkali atoms (in that case rubidium) at the cell walls can contribute to the magnetic noise with few $\mathrm{fT}/\sqrt{\mathrm{Hz}}$.

Heating of the vapor cell should generate as little magnetic noise as possible. Several methods are available for low-noise heating of the cell. First, one can heat a nonmagnetic and nonmetallic oven by directing heated compressed air through the oven. However, the electrical power requirements of the heater are high and thus it is not suitable for portable low-power sensors. Second, the vapor cell can be heated electrically; in this case, though, the currents carried by the wires cause magnetic fields and thus interfere with the measurement. However, methods to tackle the aforementioned problem exist: one can chop the currents and take the

measurements while the currents are off, or alternatively one can use AC currents with frequency much higher than the bandwidth of the magnetometer. In addition, the geometry of the current-carrying heating elements can be designed so that the generated magnetic fields cancel [41, 42]. Last, the cell can be heated optically, which eliminates the noise from the heating currents entirely [43]. The heated vapor cell has to be also thermally insulated to minimize the power loss and allow contact with a living subject.

2.3 Magnetic shielding

In this section, I will discuss the magnetic field shielding methods in general. In particular, the methods to provide suitable magnetic environments for SERF OPMs, i.e., magnetic fields less than roughly 10 nT and without significant gradients, are reviewed.

The magnetic shielding offered by bulk material occurs via two distinct processes depending on the frequency of the field: flux shunting and eddy-current cancellation [44]. For DC and near-DC fields the dominating process is flux shunting, which occurs due to higher-than-1 relative permeability of material. If we have a cylindrical shield with high relative permeability in a static magnetic field, the magnetic field lines bend due to boundary conditions imposed by the Maxwell's equations so that in the outermost layer of the shield, the magnetic field is nearly perpendicular to the surface while in the innermost layer the field is nearly tangential. Thus, the net effect is that magnetic field diverts into the shield and shunts within the shield so that only a small fraction of field penetrates the inside of the shield. The shielding efficiency of such a cylinder can be enhanced by increasing the relative permeability or by increasing the material thickness with respect to the shield diameter [44].

For AC magnetic fields, also eddy currents provide shielding. The time-varying magnetic field induces currents in the shielding material which in turn generate a magnetic field opposing the incident magnetic field and thereby decrease the field inside the shielding. The quantity describing this effect is skin depth δ, which can be obtained as follows. The propagation constant for an electromagnetic plane wave in conducting material is [44]

$$k = \sqrt{i\omega\mu(\sigma + i\omega\epsilon)}, \tag{50}$$

where ω is the angular frequency, μ and ϵ are the permeability and permittivity of the material, respectively. If the material is a good conductor, i.e., $\sigma \gg \omega\epsilon$ then the propagation constant simplifies into

$$k \approx \sqrt{i\omega\mu\sigma} = (1+i)\sqrt{\frac{\omega\mu\sigma}{2}} = \frac{1+i}{\delta}, \tag{51}$$

where

$$\delta = \sqrt{\frac{2}{\omega\mu\sigma}} \tag{52}$$

is the skin depth. The imaginary part of the propagation constant describes exponential attenuation of the field in the material; hence, δ is the length constant of

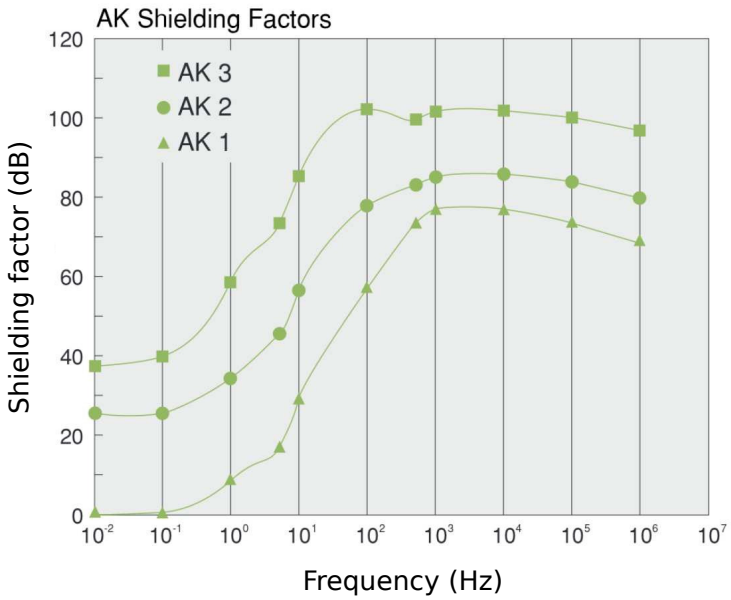

Figure 6: Shielding factors as a function of frequency for three commercially available magnetically shielded rooms. AK 1: one aluminium layer; AK 2: permalloy–aluminium layer construction; AK 3: permalloy–aluminium–permalloy layer construction. Figure is taken from the product catalog of NEC/TOCIN [45].

this attenuation. Thus, the shield provides effective attenuation of AC fields when its thickness is much larger than δ. The eddy-current shielding provided by highly conductive material can be further enhanced by increasing the diameter of the shield while keeping the thickness constant [44].

The most common way to reduce external disturbances in biomagnetic research is to perform the measurements in magnetically shielded room (MSR). The walls of an MSR consist of a variable number of layers of highly permeable material (typically mu-metal or permalloy) and highly conductive material (typically aluminium). The high permeability layers of the MSR offer shielding at low frequencies while the aluminium layers shield at higher frequencies with the mechanisms described before. The commercial and most used MSRs usually have two or three layers (from interior to exterior: permalloy–aluminium or permalloy–aluminium–permalloy) [45]. Typically, MSRs are bulky: for example, the commercial three-layer MSR has outside dimensions of $3.45\times4.45\times2.8$ m^3 and weighs 6.8 tons [45]. The shielding factors provided by the commercial MSRs are illustrated in Fig. 6, where the typical behaviour of the shielding factor is clearly visible: the shielding factor increases towards higher frequencies.

To improve the low-frequency shielding factor of an MSR, additional methods are available: shaking and active compensation [46]. In shaking, the permeability of the material (and thus also the shielding factor) is increased by applying an alternating magnetic field into the material [47]. In active compensation, the residual magnetic field inside the room is nulled by generating an opposing magnetic field [46, 48]. The

active compensation is established with a closed-loop control system which consists of magnetic field sensor(s), control electronics and a coil set surrounding the shielded volume. The electronics of such a system processes the output of the field sensors (which are typically outside the MSR) and then feed currents into the coils so that the coil-generated field opposes the measured field. Shaking can increase the shielding factor by 6 dB per shell [46] while active compensation has been shown to increase shielding factor by 35 dB at 0.1 Hz and by 20 dB at 1 Hz in one study [46] and by 40 dB at low frequencies in another study [48].

Using the aforementioned principles of shielding, a very high performance MSR has been built in Berlin [49]. It consists of seven layers of mu-metal, one layer of aluminium and an active compensation system. This MSR has shielding factors of about 97, 153 and 166 dB at frequencies 0.01, 1 and 5 Hz, respectively. The superiority of this room can be seen by comparing these values to the shielding factors of a typical commercial MSR shown in Fig. 6.

As explained before, the typical commercial MSRs do not provide sufficiently low-noise magnetic environment for the SERF OPMs. To date, suitable magnetic environments have been established by using several methods.

First, custom magnetic shields with active compensation have been made [50]. The magnetic shield in Ref. 50 is a three-layer mu-metal cylinder with an inner diameter of 1 m and length of 2.6 m. The authors reported transverse shielding factor of 77 dB and longitudinal shielding factor of 60 dB. The subject has access to the shield through a 0.6-m diameter hole that has a negligible effect on the shielding factor. In addition, they used 18 computer-controlled coils inside the shield to compensate the uniform residual fields and linear gradients.

Second, measurements have been made in the extraordinary MSR in Berlin (Refs. 8 and 51, for example). Last, SERF OPMs have been operated in commercial MSRs using compensation provided either by a set of larger coils [52] or by using smaller coils sensor-wise [53]. The compensation system of Ref. 52 consists of 18 coils wrapped inside a 1.16 m in diameter and 1.22 m long cylinder. By measuring the ambient magnetic field in the region of the OPM, the authors determined the currents in the coils so that the magnetic field was zeroed. However, the large-coil-set approach has certain disadvantages: it cannot conveniently provide simultaneous field modulations at multiple sensors for lock-in detection and it is difficult to null the fictitious magnetic fields due to the AC stark shifts at the sensors in non-planar arrays: the magnitudes of these fields are roughly the same between the sensors but the direction of the field depends on the orientation of the magnetometer and the direction of the pumping beam [53].

The sensor-wise coils solve these problems. The procedure for DC magnetic field nulling for a single magnetometer with its own compensation coils is (assuming that the magnetometer is most sensitive to y-direction): [27, 53]

- Sweep B_y and set the operating point so that the magnetometer is most sensitive, i.e., at the center of the dispersion curve (see Fig. 5).

- Apply an oscillating field $B_0 \sin(\omega t)\hat{\mathbf{e}}_\mathbf{x}$ and adjust B_z until there is no response to B_0, ensuring B_y remains at the most sensitive operating point at the sensor.

- Apply $B_0 \sin(\omega t)\hat{\mathbf{e}}_\mathbf{z}$ and adjust B_x until there is no response to B_0, ensuring B_y remains at the most sensitive operating point.
- Repeat until residual response to B_x and B_z is minimized.

However, in practical applications it is most advisable to use both large and sensor-wise coils for the nulling of the ambient field: first, bring the ambient magnetic field as close to zero as possible at the sensor site with a large coil set and then use the sensor-wise coils to null the residual fields and to provide field modulation.

3 Methods

In this section I will review the measurement setup, electronics and computational methods. The work of this thesis was roughly done in three parts. First, the static and dynamic magnetic fields inside the two MSRs of Aalto University were measured and analyzed: one MSR comprising two layers and located in the F building (MSD-2S, ETS-Lindgren Oy, Eira, Finland) and another with three layers located in the Nano house (Imedco AG, Hägendorf, Switzerland). In this thesis, these two- and three-layer MSRs are denoted as MSR-2 and MSR-3, respectively. Second, based on these measurements, a compensation coil set was designed with the help of computer simulations. Last, the static and dynamic performance of the compensation coil system was measured.

3.1 Electronics and the measurement setup

The magnetic field measurements were performed with a three-axis fluxgate magnetometer (Mag-03MC1000, Bartington Instruments, Oxford, England [54]). The fluxgate magnetometer measures the three orthogonal components of the magnetic field simultaneously and has a noise floor of 6–10 $\mathrm{pT_{rms}}/\sqrt{\mathrm{Hz}}$ at 1 Hz. The magnetometer was connected to the MEG system (Elekta Oy, Helsinki, Finland) and the data were collected with the data acquisition system of Elekta at the sampling rate of 1 kHz and pass-band of 0–200 Hz in all measurements.

The DC output voltage of the fluxgate was around 5 mV when the fluxgate was placed inside the MSR-2 while the MEG system has 24-bit analog-to-digital converters (ADCs) with an input voltage range either 1 V or 10 V. The small amplitude of the fluxgate output compared to the rather large bit step of the ADCs resulted in significant quantization noise. To tackle this problem and to reduce the root-mean-square (RMS) noise of the measurement, a three-channel amplifier was designed to amplify and filter the fluxgate output signal. The schematic diagram of one channel of the amplifier is presented in Fig. 7.

In the first stage of the amplifier, the signal is amplified with an instrumentation amplifier (AD622ANZ, Analog Devices, Norwood, USA), whose gain can be set by an external resistor R_{G_1}. By controlling with an electronic switch which one of the three resistors is connected to the amplifier, its gain can be adjusted to be 1, 10 or 100. In the second stage, the signal is filtered with a unity-gain active second-order low-pass filter, which is in the Sallen–Key configuration and built around an operational amplifier (AD711JNZ, Analog Devices). The values of the capacitors and resistors were calculated according to Ref. 55 to achieve the desired corner frequency of 200 Hz and a frequency response of a Butterworth filter. At the third stage, the DC-offset of the signal can be adjusted with a potentiometer. At the last stage, the signal is further amplified with an inverting operational amplifier (AD711JNZ), whose gain can be set to 1, 2, 10 or 100 by varying the resistance R_{G_2} with a switch. The three channels of the amplifier are all supplied by two 9-V batteries. The actual measurements were performed using a total gain of 1000 and no DC-offset compensation.

For the characterization measurements of the MSRs, the three components of the

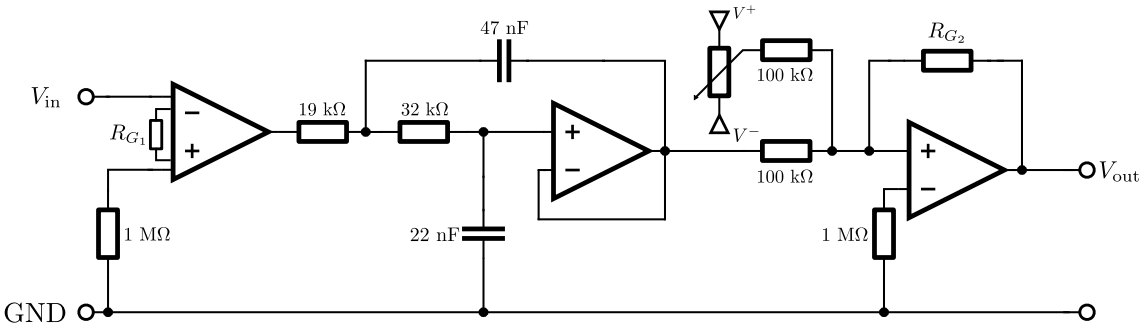

Figure 7: Circuit diagram of one channel of the designed amplifier. First, the signal is amplified with an instrumentation amplifier whose gain can be set to 1, 10 or 100 with a choice of the external resistor R_{G_1}. Second, the signal is low-pass filtered below 200 Hz with an active second-order filter. Third, the DC-offset is compensated with a potentiometer. Last, the signal is amplified with an inverting operational amplifier 1, 2, 10 or 100-fold by the choice of resistor R_{G_2}.

magnetic field were measured at nine different spatial locations in both rooms. The measurement grid comprised points distributed evenly in a cube with a sidelength of 29.3 cm; the lowest measurement points were approximately one meter above the floor. The fluxgate magnetometer was located with a custom-built frame; see Fig. 8 for an illustration of the measurement setup and the frame. Both of the MSRs house a MEG device, which occupies significant amount of space in the rooms, due to which the frame could not be placed at the center of the room. Therefore, the frame was placed in front of the MEG device in both rooms. At each point, total of 10 s of fluxgate signal was recorded and the average was taken. In addition, 200 s of fluxgate data were measured at the center of the lowest plane of the grid. From these data, the spectra were calculated using the Welch's method: the data were divided to non-overlapping 20-s segments, a Hamming window was applied to each individual segment, a discrete Fourier transform was applied and the absolute value of the complex spectrum was taken; the individual spectra were then averaged.

After the coil set was constructed, its static and dynamic performance was evaluated in MSR-2. For the DC-compensation performance, the field was first measured at a grid consisting of seven points on a cube with a sidelength of approximately 20 cm and located at the center of the coil set (six points at the centers of the faces and one point at center of the cube). The required currents in the coils that zero the field were then calculated using the procedure introduced in Sec. 3.2. The field without compensation and the current-to-field weights of the coils were estimated as averages of 1-s data. After the currents were turned on, the field was measured for 10 s at the seven points and averages were computed.

The AC performance and the proper function of the feedback loop of the compensation system was then evaluated by placing the fluxgate approximately to the center of coil set and recording 180 segments of 10 s both with and without the compensation. Then for each segment, the average and the difference between the maximum and minimum value were calculated; this difference is referred to as field

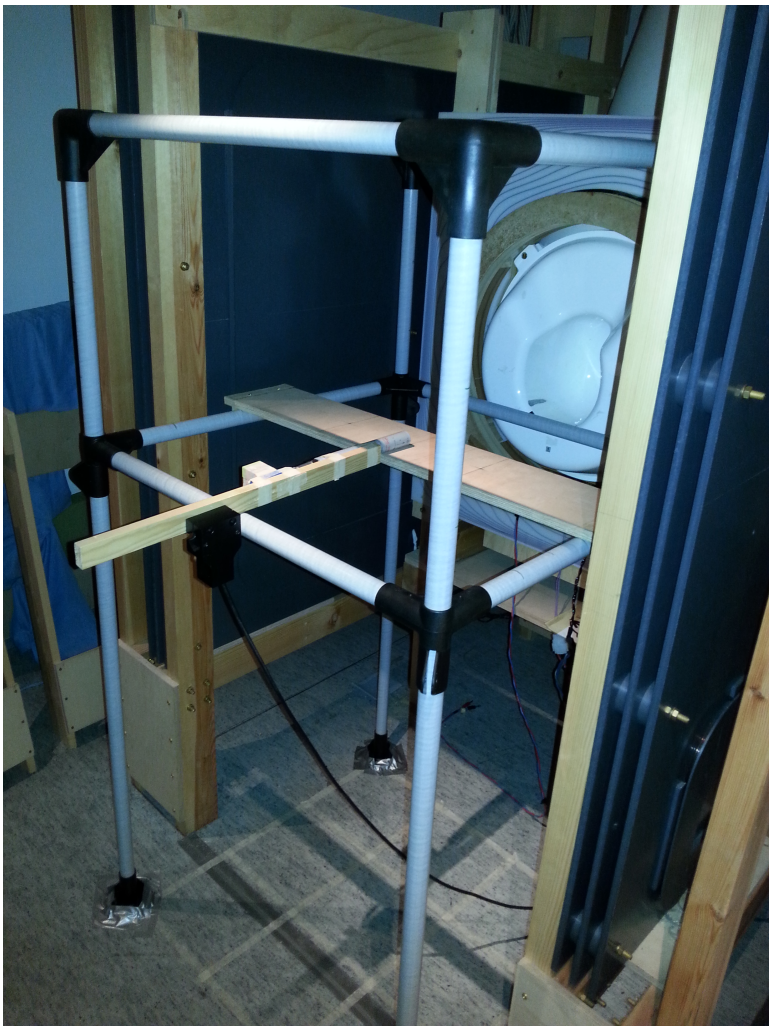

Figure 8: The setup for the measurement of the DC magnetic field inside MSR. A custom-built frame was used to fix the fluxgate at the grid positions during the measurement. The height of the plane that supports the fluxgate can be adjusted.

excursion and it describes the extrema of the field fluctuation in the given segment. The field excursion was calculated for both the raw signal and for a signal that was low-pass filtered at 5 Hz; the fluxgate signal was quite noisy so the filtering at 5 Hz was done to remove high-frequency noise and to focus on the lower-frequency interference.

The low-frequency drifts of the magnetic fields inside the MSRs and the drift introduced by the AC compensation were also quantified by measuring 200 s of data in both rooms (in MSR-2 both with and without AC compensation and in MSR-3 only without compensation). The data were then low-pass filtered at 1 Hz and the field excursion for the whole segment was calculated.

3.2 Computational methods

Linear fit to the measured field To quantify the linearity of the measured magnetic fields, a model with homogeneous components and first-order gradients was fitted to the data as follows. The model assumes that the x-component of the magnetic field at the ith field point (x_i, y_i, z_i) is given by

$$B_{x,i} = a_{x_1} x_i + a_{x_2} y_i + a_{x_3} z_i + a_{x_4}, \tag{53}$$

where a_{x_1}, a_{x_2}, a_{x_3} and a_{x_4} are constants. Writing the equation for all the N field points and casting it to the matrix form yields

$$\begin{pmatrix} x_1 & y_1 & z_1 & 1 \\ x_2 & y_2 & z_2 & 1 \\ \vdots & \vdots & \vdots & \vdots \\ x_N & y_N & z_N & 1 \end{pmatrix} \begin{pmatrix} a_{x_1} \\ a_{x_2} \\ a_{x_3} \\ a_{x_4} \end{pmatrix} = \begin{pmatrix} B_{x,1} \\ B_{x,2} \\ \vdots \\ B_{x,N} \end{pmatrix} \Leftrightarrow \mathbf{R}\mathbf{a}_\mathbf{x} = \mathbf{B}_\mathbf{x} \tag{54}$$

from which the least-squares solution for the coefficient vector $\mathbf{a_x}$ is obtained. The same procedure is then applied to get $\mathbf{a_y}$ and $\mathbf{a_z}$. The coefficients in the vectors $\mathbf{a_x}$, $\mathbf{a_y}$ and $\mathbf{a_z}$ then constitute the linear fit. The magnetic field given by the fit can be evaluated at an arbitrary point (x, y, z) as

$$\begin{pmatrix} \tilde{B}_x \\ \tilde{B}_y \\ \tilde{B}_z \end{pmatrix} = \begin{pmatrix} a_{x_1} & a_{x_2} & a_{x_3} & a_{x_4} \\ a_{y_1} & a_{y_2} & a_{y_3} & a_{y_4} \\ a_{z_1} & a_{z_2} & a_{z_3} & a_{z_4} \end{pmatrix} \begin{pmatrix} x \\ y \\ z \\ 1 \end{pmatrix} \Leftrightarrow \tilde{\mathbf{B}} = \begin{pmatrix} \mathbf{a_x}^\mathrm{T} \\ \mathbf{a_y}^\mathrm{T} \\ \mathbf{a_z}^\mathrm{T} \end{pmatrix} \begin{pmatrix} x \\ y \\ z \\ 1 \end{pmatrix}. \tag{55}$$

Eq. (55) can be written in another way to reveal the meaning of the coefficients:

$$\begin{pmatrix} \tilde{B}_x \\ \tilde{B}_y \\ \tilde{B}_z \end{pmatrix} = \begin{pmatrix} a_{x_1} & a_{x_2} & a_{x_3} \\ a_{y_1} & a_{y_2} & a_{y_3} \\ a_{z_1} & a_{z_2} & a_{z_3} \end{pmatrix} \begin{pmatrix} x \\ y \\ z \end{pmatrix} + \begin{pmatrix} a_{x_4} \\ a_{y_4} \\ a_{z_4} \end{pmatrix} \tag{56}$$

$$= \begin{pmatrix} \frac{\partial B_x}{\partial x} & \frac{\partial B_x}{\partial y} & \frac{\partial B_x}{\partial z} \\ \frac{\partial B_y}{\partial x} & \frac{\partial B_y}{\partial y} & \frac{\partial B_y}{\partial z} \\ \frac{\partial B_z}{\partial x} & \frac{\partial B_z}{\partial y} & \frac{\partial B_z}{\partial z} \end{pmatrix} \begin{pmatrix} x \\ y \\ z \end{pmatrix} + \begin{pmatrix} B_x^0 \\ B_y^0 \\ B_z^0 \end{pmatrix} \tag{57}$$

$$= \frac{d\mathbf{B}}{d\mathbf{x}}\mathbf{x} + \mathbf{B}^0. \tag{58}$$

The coefficients thus represent the first-order field gradients and the homogeneous components. Therefore, the method provides direct means to estimate the strengths of the field gradients in the rooms.

The deviation of the measured field from this model can be subsequently assessed by computing the root-mean-square error (RMSE) of the fit of the field components:

$$\mathrm{RMSE}_i = \sqrt{\frac{\sum_{j=1}^{N} (B_{i,j} - \tilde{B}_{i,j})^2}{N}}, \tag{59}$$

where $i \in \{x, y, z\}$ and N is the number of measurement points.

Computation of the magnetic field of a coil system Arbitrarily-shaped coil can be handled by segmenting the coil to sufficiently small line segments and then superposing the fields of the individual segments. Assuming that current I is constant in each element, the magnetic field from a single element starting from $\mathbf{r'_1}$ and ending to $\mathbf{r'_2}$ can be calculated efficiently as [56]

$$\mathbf{B}(\mathbf{r}) = \frac{\mu_0 I}{4\pi} \frac{c_1 + c_2}{c_1 c_2} \frac{\mathbf{c_1} \times \mathbf{c_2}}{c_1 c_2 + \mathbf{c_1} \cdot \mathbf{c_2}}, \tag{60}$$

where $\mathbf{c_i} = \mathbf{r'_i} - \mathbf{r}$ and $c_i = |\mathbf{c_i}|$.

Magnetic field inhomogeneity The inhomogeneity of the magnetic field (IH), that is produced by the coil set, can be quantified by calculating the relative error of the field inside the coil set to the field at the center of the coil system

$$\mathrm{IH} = \frac{||\mathbf{B}_{\mathrm{ref}} - \mathbf{B}||}{||\mathbf{B}_{\mathrm{ref}}||}, \tag{61}$$

where $\mathbf{B}_{\mathrm{ref}}$ is the field at the center of the coil set and $||\cdot||$ is the Euclidean norm.

Computation of the required currents in the coils When the shapes and positions of the coils and field points are fixed, the magnetic field at P points is related to the currents of the K coils via a linear mapping

$$\mathbf{B} = \mathbf{M}\mathbf{I}, \tag{62}$$

where $\mathbf{M}$ is the current-to-field transfer matrix and the dimensions of $\mathbf{B}$, $\mathbf{M}$ and $\mathbf{I}$ are $3P \times 1$, $3P \times K$ and $K \times 1$, respectively. The elements of matrix $\mathbf{M}$ are easily calculated by using Eq. (60) with unit currents. The currents are then determined as the least-squares solution to Eq. (62).

The performance of the DC-field compensation of the coil set can then be simulated with the use of Eq. (62). To this end, the measured fields were interpolated to a $10 \times 10 \times 10$ grid sampled uniformly in a cube with a sidelength of 20 cm. Then, the currents in the coils were calculated from Eq. (62) and the field produced by the coil set was computed in the grid.

The transfer matrix $\mathbf{M}$ can be also measured experimentally: the three rows of the matrix corresponding to one point can be estimated by fixing the fluxgate to that point and then measuring the magnetic field caused by a predetermined current in each coil. By iterating the procedure for each point, the full transfer matrix $\mathbf{M}$ can be constructed. The compensation currents are then given by the least-squares solution.

4 Results

I will review the obtained results in this section. In the first part, the results characterizing the magnetic fields inside the two MSRs (MSR-2 and MSR-3) of Aalto University are presented. The second part deals with the construction and design of the compensation system: the motivation behind the chosen coil design is given and the performance of the coil set is evaluated with simulations; in addition, the feedback loop of the active compensation is presented. In the third part, the performance results of the designed compensation system are reviewed.

4.1 Characterization of the magnetically shielded rooms

The measured DC fields at both MSRs together with their linear models are presented in Fig. 9. As can be seen in the figure, there is a huge difference between the magnetic field amplitudes between the two MSRs: in MSR-3, the field is below 5 nT while in MSR-2 it ranges from 80 to 95 nT. Visual inspection also shows that the linear model of the magnetic fields fits to the measurements quite well. The RMSEs of the fits are for the x-, y- and z-components of the field 1.12, 1.19, 0.75 nT for the MSR-2 and 0.18, 0.27 and 0.16 nT for the MSR-3, respectively.

The estimated Jacobian matrices (units nT/m) and homogeneous components (in nT) for the MSR-2 are

$$\frac{d\mathbf{B}}{d\mathbf{x}} = \begin{pmatrix} -0.51 & -1.54 & -5.94 \\ -0.58 & 37.82 & -4.15 \\ 11.12 & 2.96 & -38.49 \end{pmatrix}, \quad \mathbf{B}^0 = \begin{pmatrix} 9.80 \\ -90.75 \\ 67.69 \end{pmatrix} \tag{63}$$

while the corresponding metrics for the MSR-3 are

$$\frac{d\mathbf{B}}{d\mathbf{x}} = \begin{pmatrix} 5.42 & 1.22 & 0.88 \\ 1.66 & -1.06 & 0.41 \\ -0.61 & 1.04 & -5.97 \end{pmatrix}, \quad \mathbf{B}^0 = \begin{pmatrix} -1.98 \\ -0.86 \\ 9.40 \end{pmatrix}. \tag{64}$$

The two strongest gradients are in the diagonal of the Jacobian in both rooms: in MSR-2 they are $\partial B_y/\partial y = 37.8$ nT/m and $\partial B_z/\partial z = -38.5$ nT/m and in MSR-3 $\partial B_x/\partial x = 5.4$ nT/m and $\partial B_z/\partial z = -6.0$ nT/m. However, in MSR-2 there is also a rather large off-diagonal gradient $\partial B_z/\partial x = 11.1$ nT/m. Notably, the field gradients and homogeneous components are roughly an order of magnitude higher in MSR-2 than in MSR-3.

In Fig. 10, 30-s readings of unfiltered fluxgate signal (bandwidth 0–200 Hz) are shown together with signals low-pass filtered below 5 and 20 Hz for both rooms. The unfiltered fluxgate signal is rather noisy as the figure shows but the filtered signals reveal field drifts already from this short segment of data; for example, B_z of MSR-2 at 10.5 s and 19.5 s. The standard deviations of the unfiltered time traces of x-, y- and z-components are 0.39, 0.33 and 0.61 nT for MSR-2 data and 0.55, 0.61 and 0.60 nT for MSR-3 data.

The spectra of the magnetic field components in both MSRs are presented in Fig. 11. The spectra between the different components and rooms look rather similar.

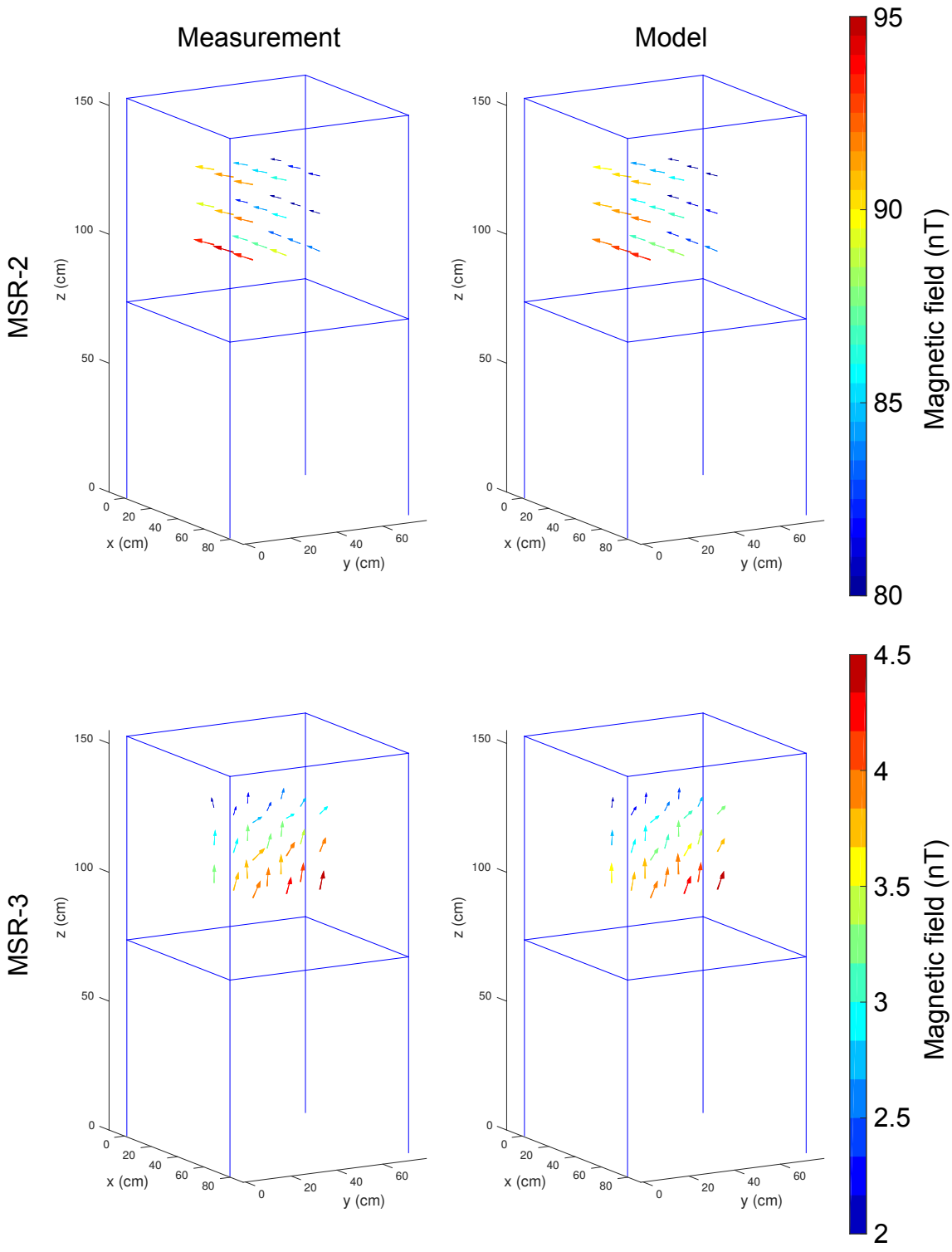

Figure 9: The measured DC magnetic fields inside two MSRs of Aalto University (MSR-2 is composed of two layers while MSR-3 comprises three layers) and their linear models. The custom-built frame that was used to fix the fluxgate is shown schematically (see Fig. 8).

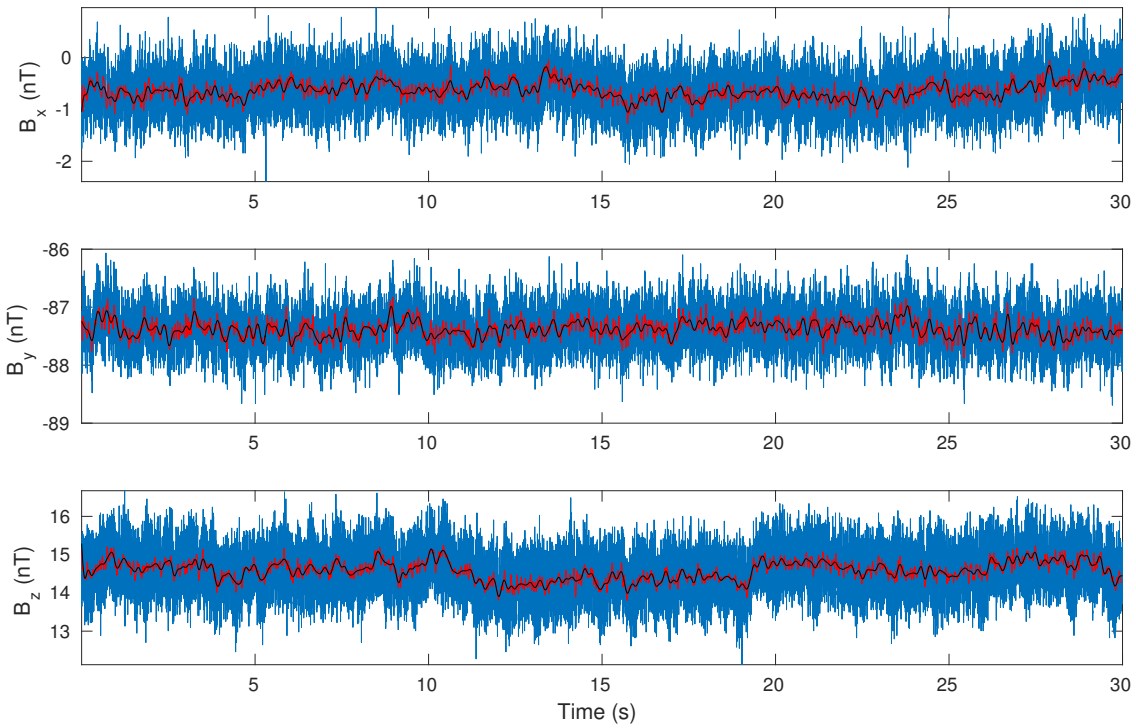

(a)

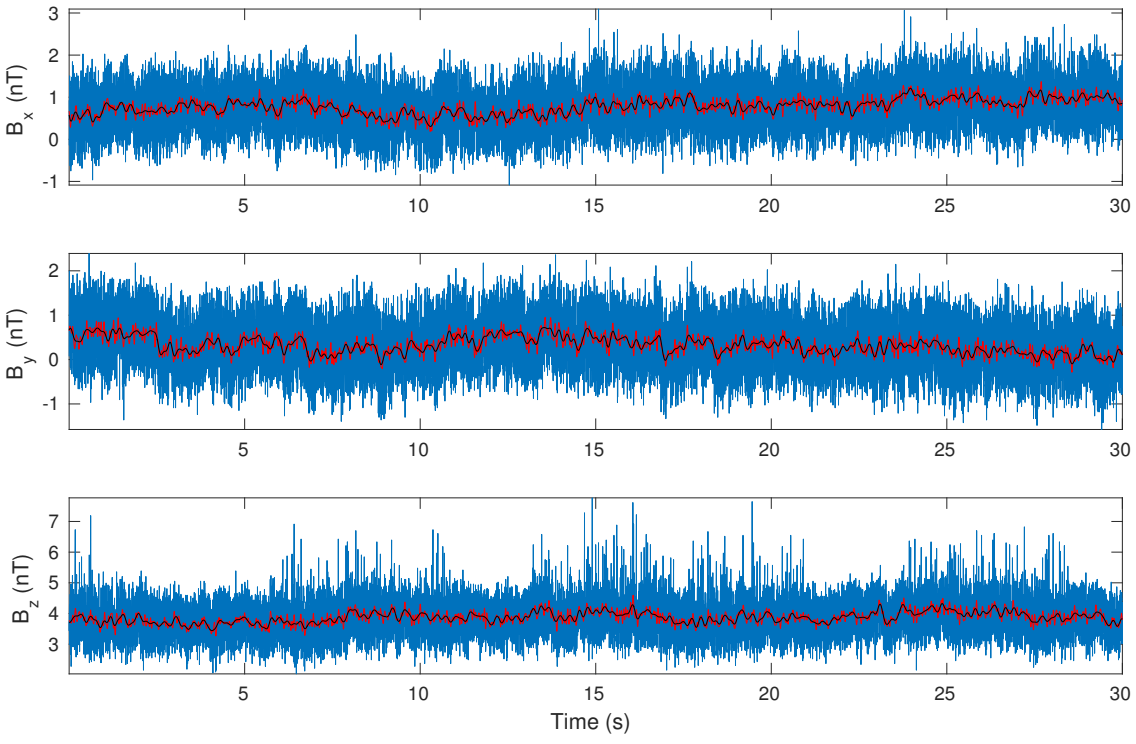

(b)

Figure 10: Exemplary 30-s length recordings of raw fluxgate signal (bandwidth 0–200 Hz; blue) together with signals low-pass filtered at 5 Hz (black) and 20 Hz (red) for the two-layer MSR (a) and three-layer MSR (b).

The spectra show the characteristic $1/f$ frequency dependence with peaks at the mains frequency and its harmonics (50, 100 and 150 Hz); the white noise region starts approximately at 30 Hz. The similarity of the spectra suggests that the main noise contributions to the measurements come from electronics. However, some differences can be seen: the densities at the smallest frequencies (≤ 0.1 Hz) are higher in the MSR-2 spectra and the spectrum of z-component of the field in MSR-2 shows a local maximum between 0.1 and 1 Hz.

The field excursions for the 200-s data that were low-pass filtered at 1 Hz were 1.12, 0.95 and 1.39 nT for the x-, y- and z-components of the field in MSR-2. The corresponding values were 0.83, 0.83 and 0.77 nT for the field components in MSR-3.

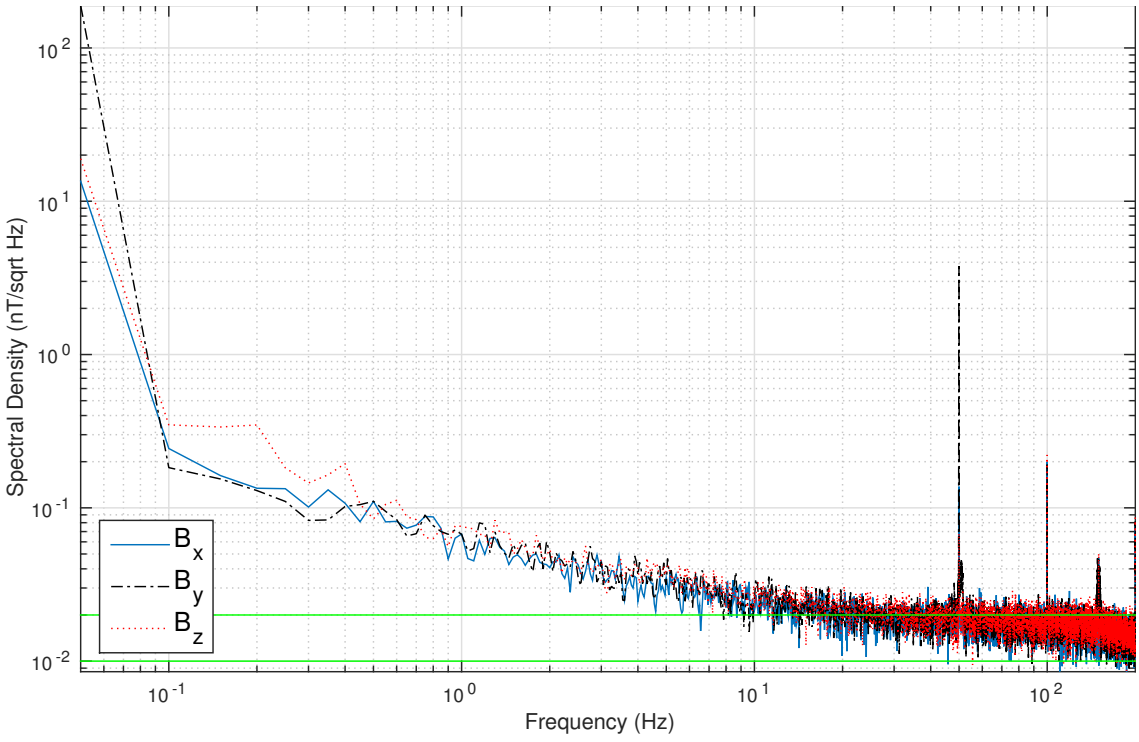

(a)

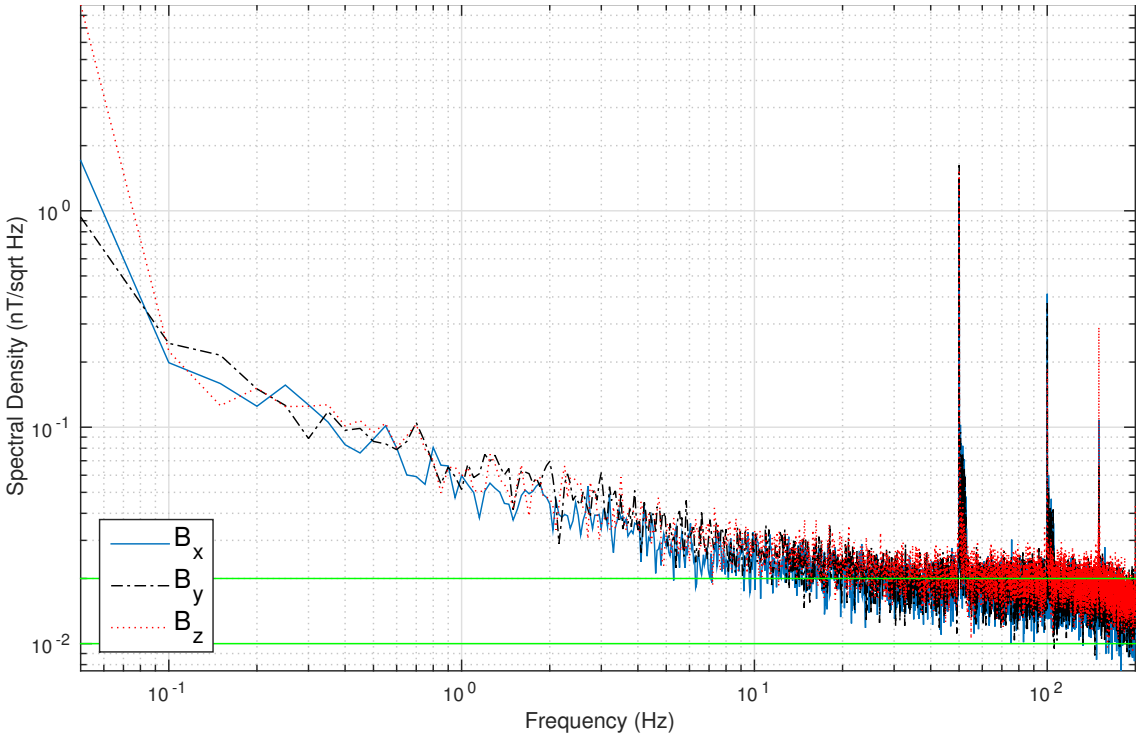

(b)

Figure 11: The spectral densities of the magnetic field components in both MSRs of Aalto (two-layer MSR (a); three-layer MSR (b)). The specified upper and lower limit of the noise floor of the fluxgate magnetometer are plotted in green.

4.2 Design and construction of the compensation system

The design criteria for the magnetic field compensation system were:

- It should movable; in particular, it should fit through the doors of the MSRs which are approximately one meter wide.
- Subject's head should fit into the system and the system should be as open as possible (for example, without any obstacles blocking the visual field in case visual stimuli are used).
- It should be able to reduce the DC-field below 10 nT in a head-sized volume.
- It should actively compensate low-frequency interference; the field drifts should not exceed ± 2 nT.

The coil set was decided to be built on a cube with a sidelength of 70 cm and 80 cm above the floor; the frame for the coil set was the same that was used to conduct the fluxgate measurements (see Fig. 8). The sidelength of 70 cm was chosen because of the space restrictions in the MSR-2 which houses a hybrid MEG–MRI system; a cube of $(70\ \mathrm{cm})^3$ was the largest object that could be moved freely in the room although the door opening would have allowed a somewhat larger system. Cubical shape was chosen because of the ease of its construction.

This kind of a shape imposes some limits for the coils. For producing homogeneous compensating fields, the coils are usually in the so-called Helmholtz configuration (see Refs. 57, 58, 59 and 60, for example), which means that the spacing between two coils is one radius for circular coils and 0.5445 times the sidelength for rectangular coils [61, 62]. In the Helmholtz configuration, the first- and second-order spatial derivatives of the field are zero at the center of the coil set; other more complex coil setups (involving three or more coils) that null higher-order derivatives and produce higher volumes of a homogeneous field have also been constructed (for a review, see Ref. 62). Despite of its benefits, the Helmholtz configuration does not suit our purposes: if we want, for example, the subject to have 50 cm of free space in the coil system (50 cm would then be also the spacing of the coils) the coils should be about 90 cm wide and the coil system could not fit in MSR-2. Therefore, rectangular coils with 70 cm sidelength were placed on the sides of the $(70\text{-cm})^3$ cube of the frame and additional smaller homogenizing rectangular coils were introduced on the sides of the cube. In Ref. 63, the dimensions and ampere-turns of an optimal solution (in the sense of field homogeneity) of such a coil system have been calculated. The authors found that the width of the field homogenizing coils should be 0.75 times the width of the main coils and they should carry current 0.58 times the current in main coils to the opposite direction. The schematic of such a coil system is presented in Fig. 12. The disadvantage of the setup is that the required currents are higher than in the case of pure Helmholtz coils. On the other hand, the coil setup gives slightly higher field homogeneity than the Helmholtz coils [63].

In Fig. 13a the field inhomogeneity in the central axis is plotted and in Fig. 13b the inhomogeneity is visualized in a volume lying at the center of the coils. Along

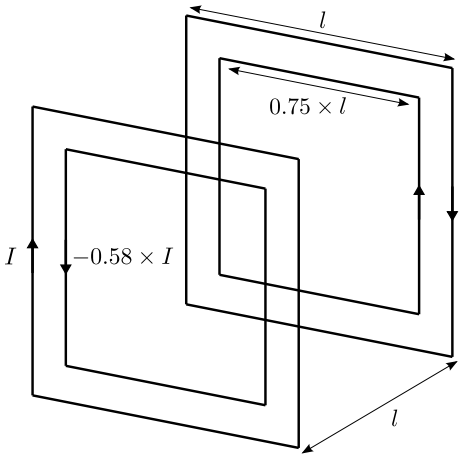

Figure 12: A schematic of the coils used in the compensation system. Coils with width l carrying current I at the outer coil and $-0.58 \times I$ at the inner coil are separated by distance l. The two coils on the same side are coaxial; the width of the inner coil is $0.75 \times l$.

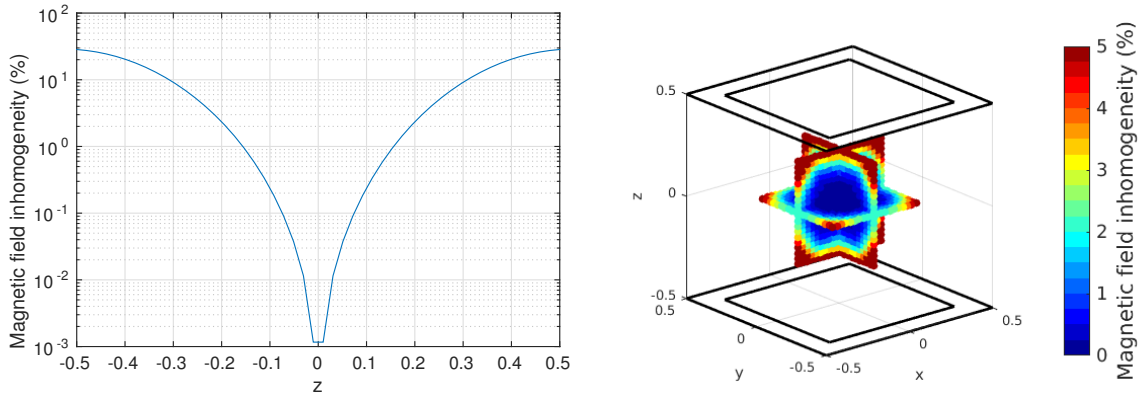

Figure 13: Field inhomogeneity of the coil setup. (a) Field inhomogeneity along the central axis of the coils; (b) field inhomogeneity in a volume at the center of the coils. The coils are positioned at $z = -0.5$ and $z = 0.5$; the units of the coordinates are arbitrary.

the central axis of the coils, the field inhomogeneity is less than 1% in a 20-cm line located at the center of the system. In a volume of $(20\ \text{cm})^3$, the maximum magnetic field inhomogeneity is about 2%.

With three orthogonal sets of the aforementioned coils, the static compensation performance of the coil set was tested. Fig. 14 shows the simulated magnetic fields after compensation for both rooms. The simulation shows that the compensation system should be able to reduce the field to below 3 nT and 0.9 nT in a $(20\text{-cm})^3$ volume at the center of the system in MSR-2 and MSR-3, respectively. The figure shows that the largest residual field values are on the edges of the volume. Near the center of the volume field values as small as about 2 nT in the two-layer MSR and

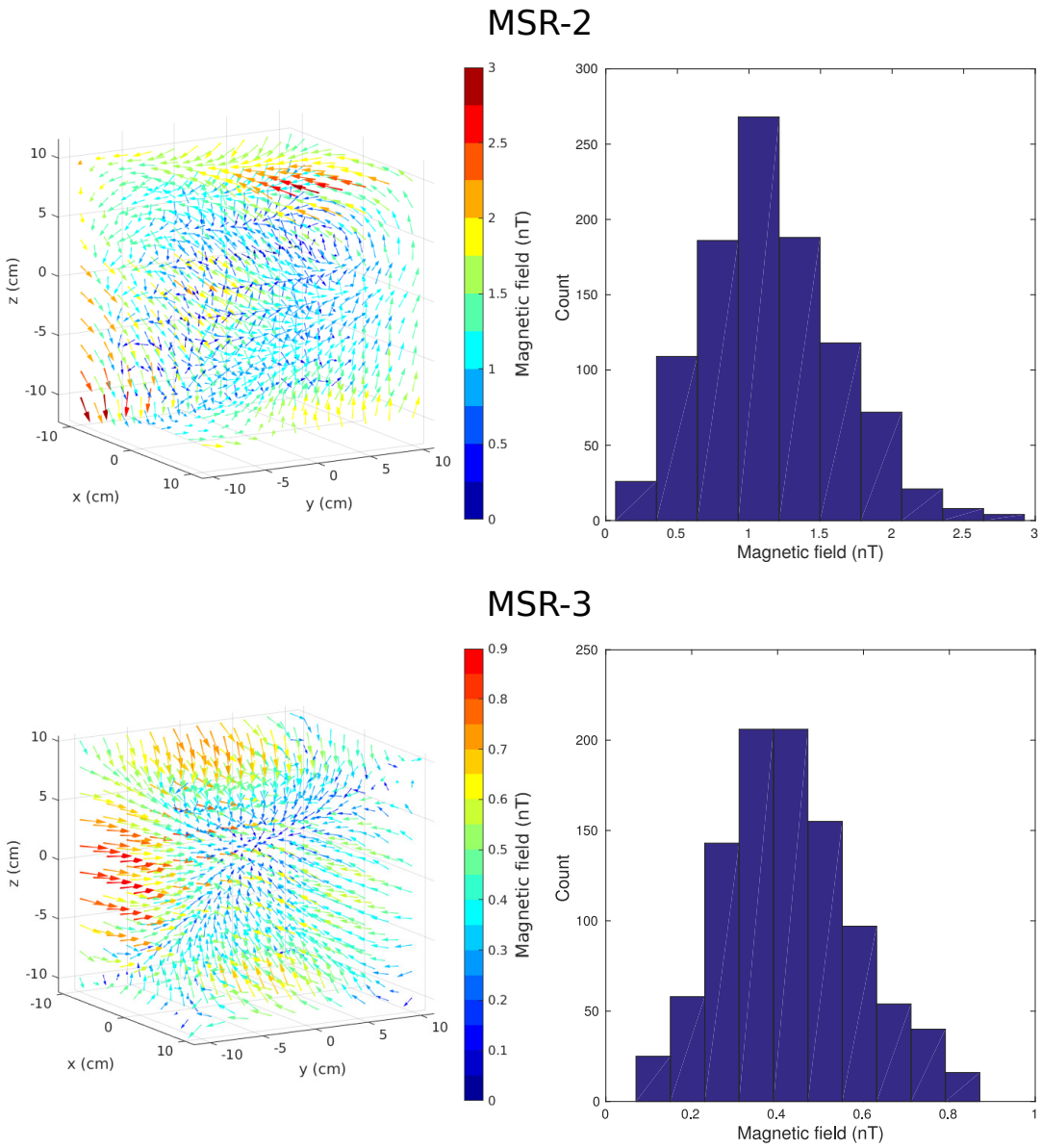

Figure 14: The simulated residual magnetic fields in a $(20\text{-cm})^3$ volume inside the coil set. Histograms show the distribution of the magnetic field amplitudes across the measurement points. Top row: two-layer MSR-2; bottom row: three-layer MSR-3.

0.6 nT in the three-layer MSR can be achieved.

The constructed compensation coil set is presented in Fig. 15. It consists of six individual coils, which can be controlled with a computer; the coils are in the setup described before (see Fig. 12). The larger and smaller coil constituting one coil are in series; the coils are wounded so that in the smaller coil flows opposite current than in the larger coil. The ampere-turns of the coils are 14 and 8, which gives ratio of 0.57 which is close to the ideal ratio of 0.58. The coils are connected to the Elekta MEG system electronics with a SCSI-cable. The maximum absolute output voltage that Elekta system can provide is 10 V which translates into a current of about 20

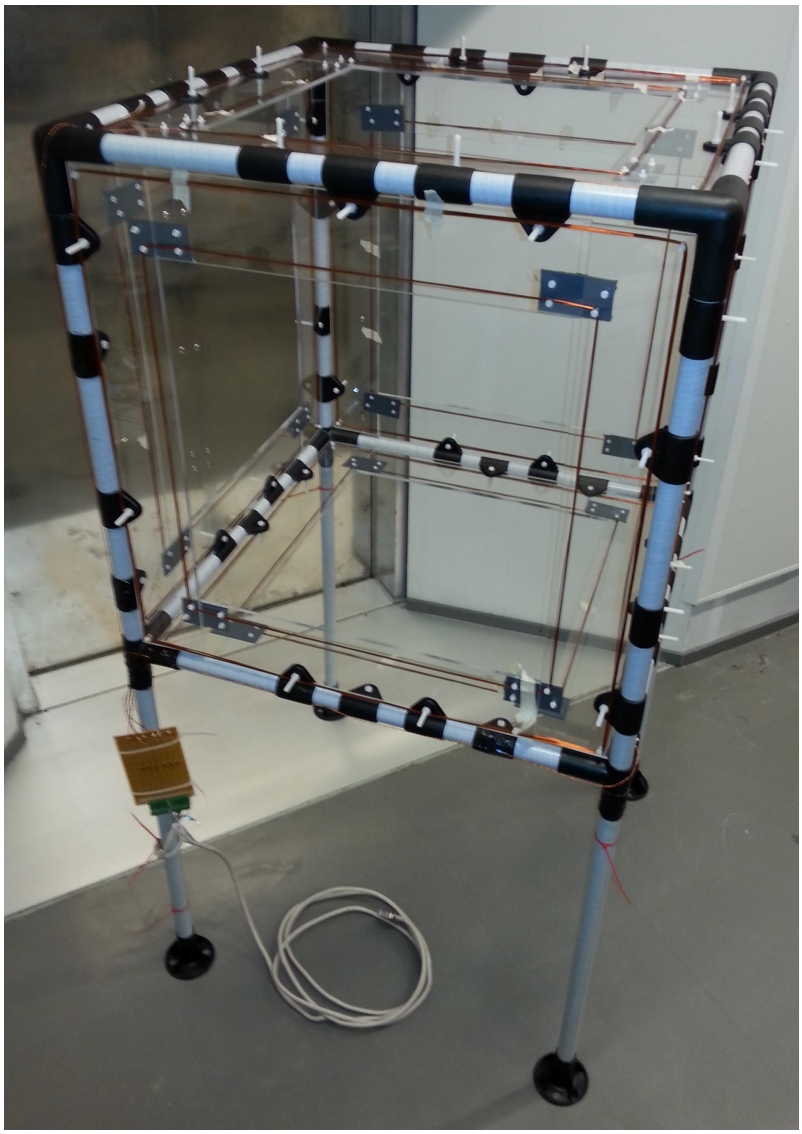

Figure 15: Photograph of the constructed compensation coil set. The coil set consists of six individual computer-controlled coils each of them consisting of two rectangular coils (one larger and one smaller) in series.

mA in the coils due to limitations imposed by the output impedance and operational amplifiers of the electronics of the system. The maximum field that the coil pairs can produce is then approximately ±160 nT at the center of the compensation system.

The block diagram of the feedback loop for the active compensation is shown in Fig. 16. Its operation is described here at a general level. The sensors measure the magnetic field, which is a superposition of the magnetic fields generated by various sources, e.g., the currents in the brain, currents in the compensation coils and numerous sources of interference, in various spatial locations. If a fluxgate magnetometer is used as the detector, it is advantageous to amplify and filter the signal analogically (see Sec. 3.1); these optional analogue stages then constitute the first blocks in the diagram. The sensor signals are then converted into digital form

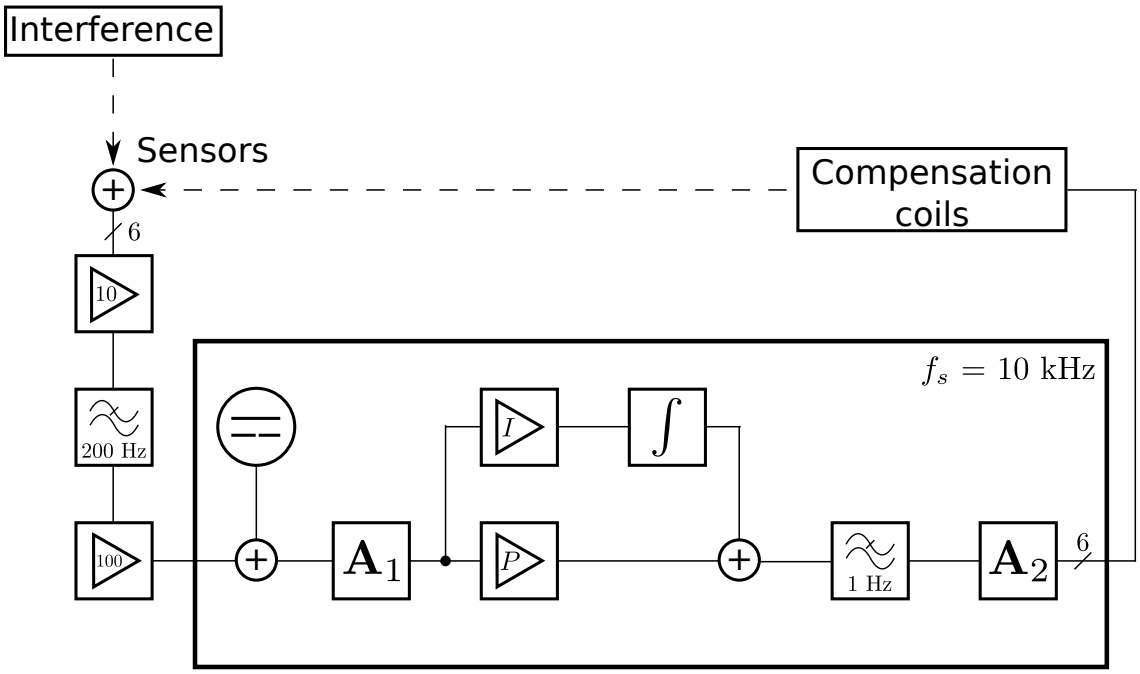

Figure 16: Block diagram of the active compensation feedback loop. Couplings via magnetic field are shown in dashed arrows and the box shows the digital part of the loop.

and the rest of the processing is performed digitally at the sampling frequency of 10 kHz. In the first stage of the digital processing, offsets of the signals can be adjusted. Then the signal vector is multiplied with matrix $\mathbf{A}_1$ producing the control variables which are inputted to the proportional-integral (PI) controller. The output of the PI controller is subsequently low-pass filtered at 1 Hz and transformed into coil current values by multiplication with matrix $\mathbf{A}_2$. The very low cut-off frequency low-pass filter was implemented since only the compensation of low frequency signals is desired; in this way, for example, the interesting brain signals remain mostly intact. The coil current values are then converted to analog form and fed into the compensation coils.

The digital part of the feedback loop is based on an existing implementation in the Elekta MEG system and runs on a Freescale DSP56321 (NXP Semiconductors, Eindhoven, The Netherlands) digital signal processor (DSP). Both the PI controller and the low-pass filter were programmed in assembly while the rest of the code in C. The normalized cut-off frequency of the low-pass filter is 0.0002 and thus its implementation is not trivial due to the finite precision of the DSP. The DSP uses 24-bit fixed-point arithmetic with 56-bit accumulator. To tackle finite-word-length effects, the employed IIR filter was realized using a delta operator in direct-form II transposed (DFIIt) structure composed of three second-order sections (see Ref. 64 and Appendix A). The DFIIt delta structure has been shown to yield excellent roundoff noise performance [64]. However, since the normalized cut-off frequency is extremely low in this implementation, there were still some concerns about the performance of the filter. As the cut-off frequency decreases also the filter coefficients

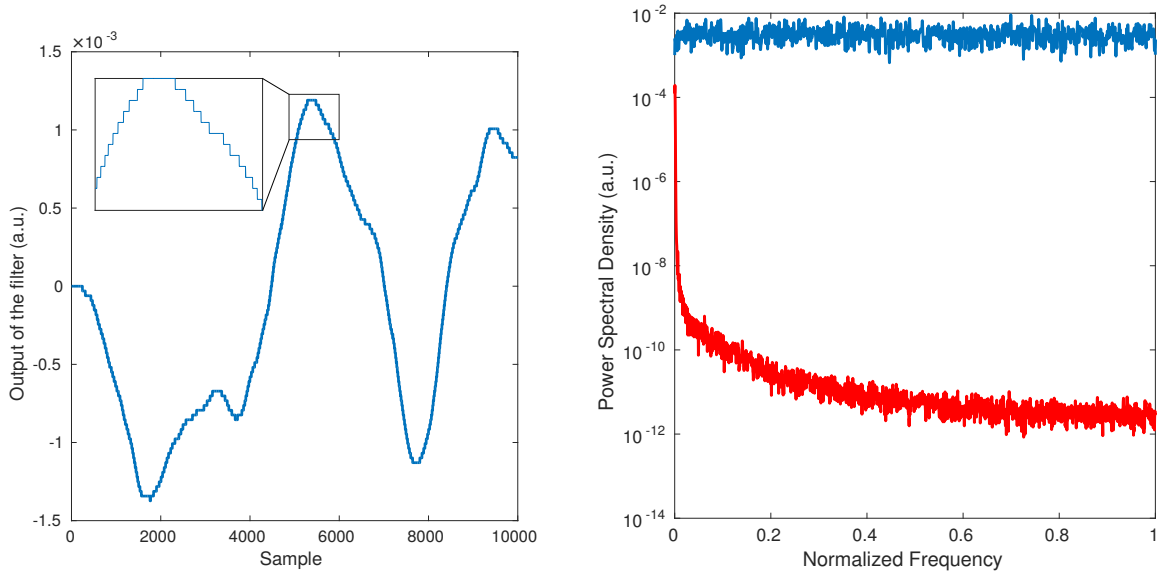

(a) (b)

Figure 17: An examplary response of the simulated direct-form II transposed delta operator IIR filter to white noise. (a) The output of the filter; inset shows the quantization of the output. (b) The spectrum of filtered white noise (red); the spectrum of the input white noise (blue).

tend to zero and the 24-bit word may not suffice for accurate representation of the coefficients. Another concern was whether the roundoff noise of the filter was acceptable.

To answer these questions, simulations were performed in Matlab using 24-bit fixed-point arithmetics. The structure and operation of the DFIIt delta operator filter were implemented and the arithmetical operations were configured to mimick the arithmetics of DSP56321. White noise was input to the filter and the output response and its spectral density were calculated. An example of one run with 10 000 samples is depicted in Fig. 17. The simulations showed that the filter can be realized; however, most of the filter coefficients are presented with only one or two bits and, thus, the cut-off frequency may deviate significantly from 1 Hz.

4.3 Performance of the compensation system

The magnetic field at seven points at the center of the coil set before and after DC compensation is shown in Fig. 18. Also the field pattern obtained by simulating the compensation field of the coil set is shown. Without compensation the field amplitudes ranged from 90 to 100 nT while with compensation the amplitudes varied from 4 to 8 nT. Thus, with DC compensation the field can be reduced by a factor slightly better than 10. The figure also shows that the residual field has an approximately opposite orientation to the field without compensation. The simulated field amplitudes range from 0.1 to 5 nT and are thus smaller than the experimentally obtained values. The simulated field pattern is also different from the pattern of the measured compensation field.

Ten-second time traces of the fluxgate signal with AC field compensation are shown in Fig. 19. The data show that the feedback loop can zero the field reasonably well; nonetheless, small deviations of the order ± 0.5 nT from zero occur in all channels.

The average fields without and with the active compensation as a function of the 10-s window index are presented in Figs. 20 and 21, respectively. The average field with the compensation is less than 0.1 nT for 84%, 100% and 88% of the time windows for x-, y- and z-components, respectively. The average field with compensation shows some fluctuations but no clear trends are visible. The standard deviations of the average fields with compensation are 0.1, 0.04 and 0.09 nT for x-, y- and z-components, respectively. Without the active compensation, there are clear field drifts visible in the averages. The values of the average field are in 1 nT range from each other without active compensation while the standard deviations of the average fields are 0.21, 0.19 and 0.15 nT for x-, y- and z-components, respectively.

The histograms of the field-excursion values are shown in Fig. 22 both with and without the compensation. The histograms are quite similar irrespective whether the compensation is on or off. For the unfiltered data (bandwidth 0–200 Hz), the values of the field excursion are less than about 5 nT and for the low-pass filtered data they are less than 2 nT. On average, the unfiltered field excursions are largest for the z-component of the field and smallest for x-component: the averages are 2.9, 3.6, 4.1 nT without compensation and 3.1, 3.5 and 4.2 nT with compensation for the x-, y- and z-components of the field, respectively. While for the filtered data, the average excursions are 0.7, 0.8 and 1.0 nT without compensation and 1.0, 0.8 and 1.1 nT with compensation for the x-, y- and z-components, respectively. The field excursion values for the 200-s data segment, which was low-pass filtered at 1 Hz, with the active compensation were 1.37, 0.60 and 1.74 nT for the x-, y- and z-components of the field, respectively.

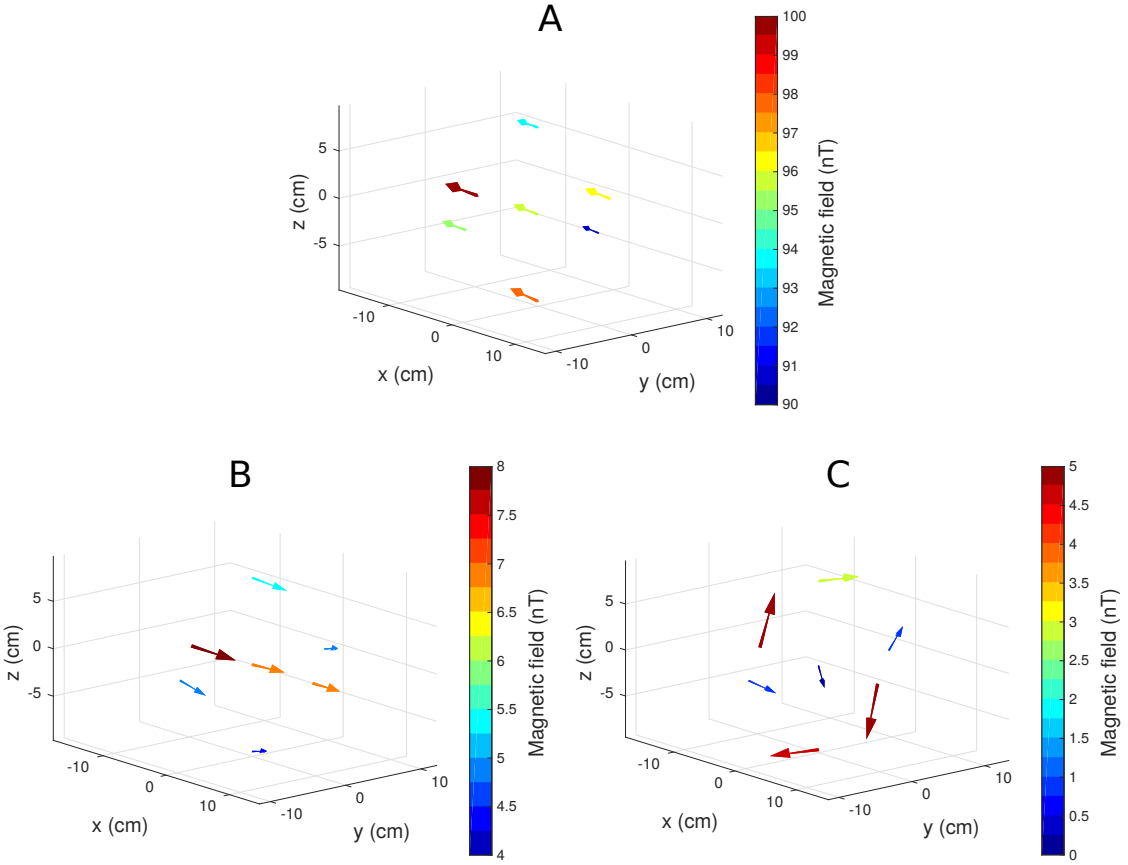

Figure 18: The DC compensation performance of the coil system. (A) The static magnetic field inside the coil set in the two-layer MSR; (B) the measured magnetic field after the DC compensation is turned on; (C) the magnetic field pattern obtained by simulations.

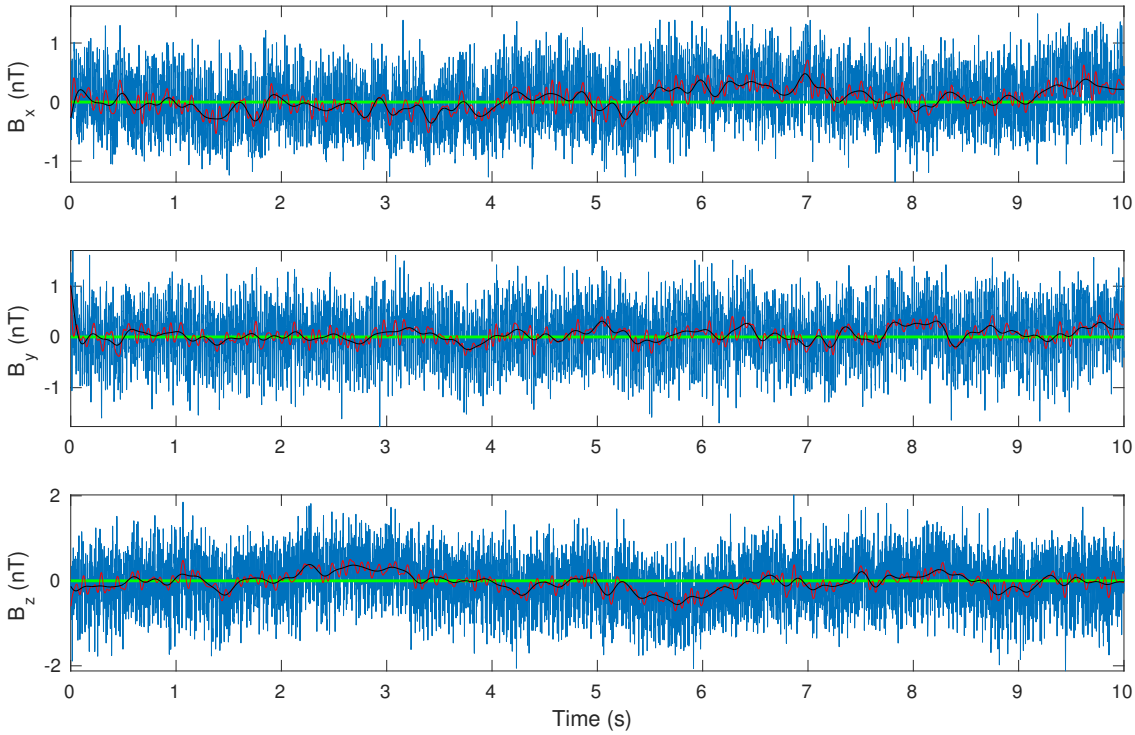

Figure 19: Ten-second time traces of the fluxgate signal with the feedback loop of the compensation system active. Raw fluxgate signal (bandwidth 0–200 Hz; blue) together with signals low-pass filtered at 5 Hz (black) and 20 Hz (red).

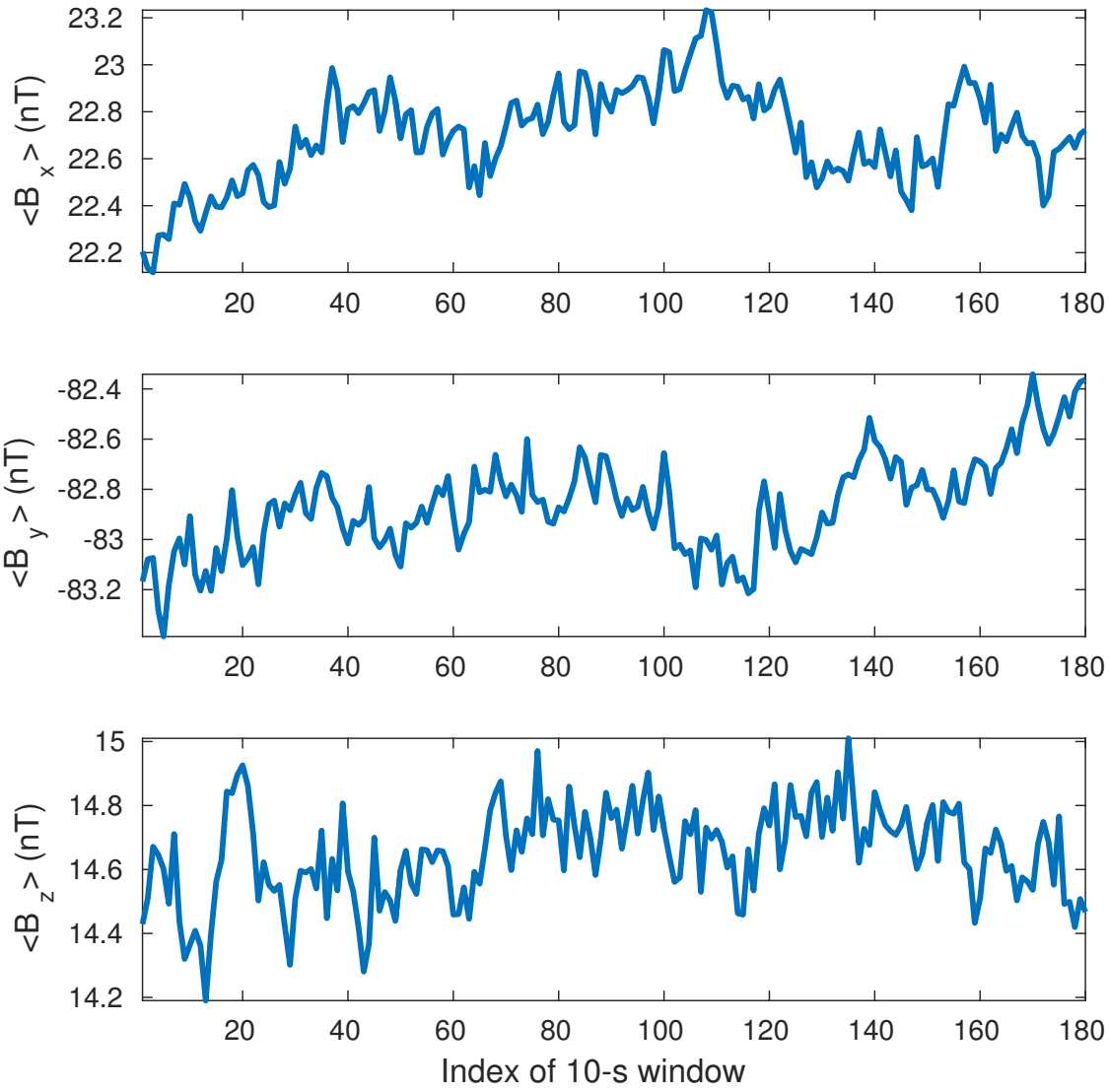

Figure 20: Ten-second averages of the field in MSR-2 without active compensation. The index refers to the 10-s time windows.

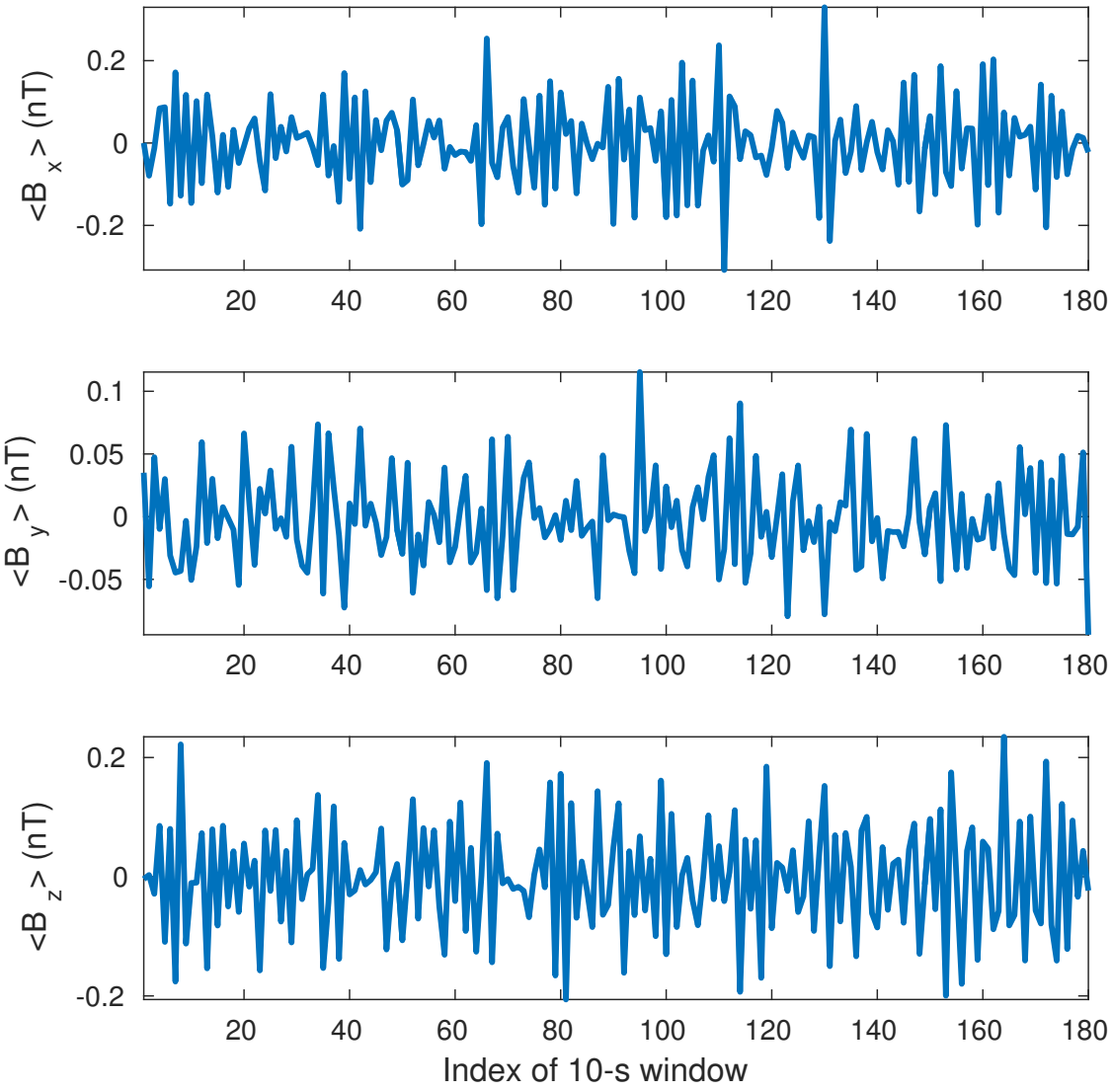

Figure 21: Ten-second averages of the field in MSR-2 recorded with the active compensation.

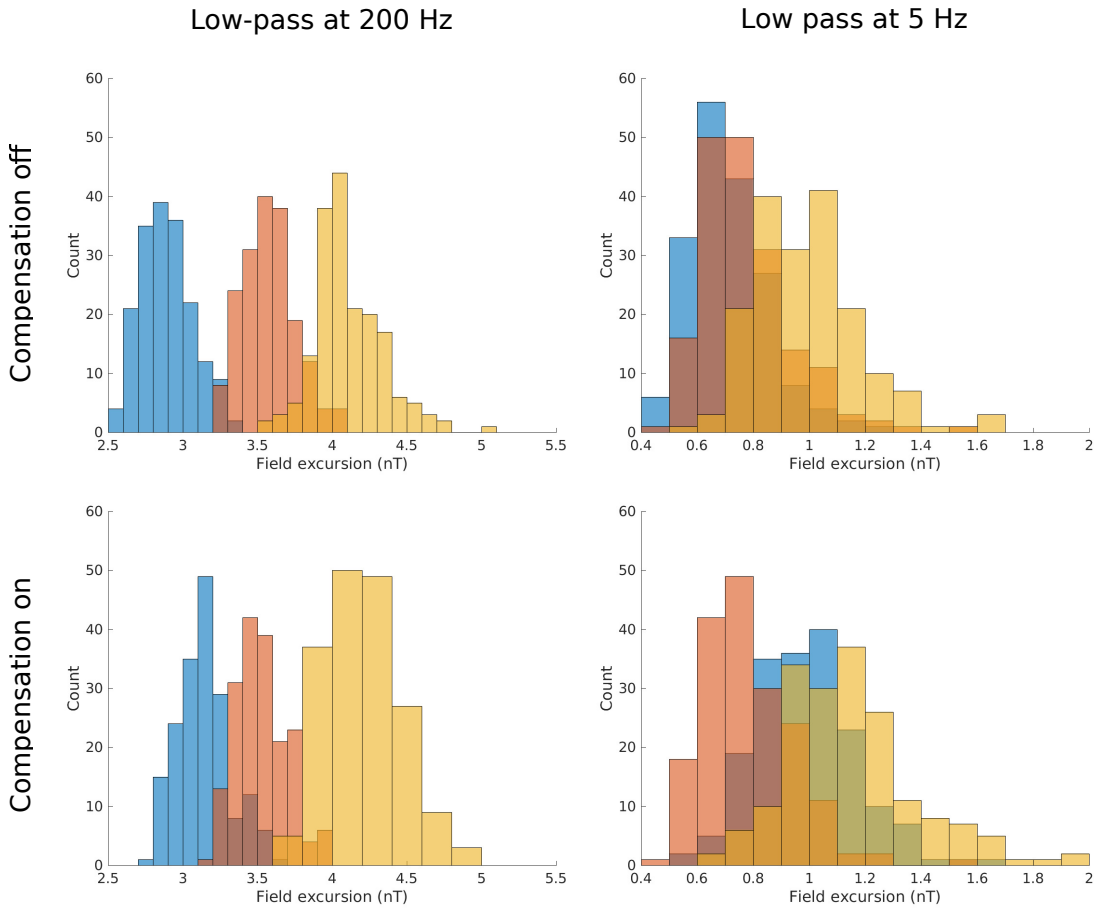

Figure 22: The field excursion calculated both with and without the active compensation for the 180 windows of 10 s. x-component of the field (blue); y-component (red); z-component (yellow). Other colours denote overlapping histograms.

5 Discussion

The aim of this thesis was to establish suitable magnetic environment for operating SERF OPMs in Aalto University. The work of the thesis was done in three parts. First, the remanent magnetic fields inside the two- and three-layer MSRs, denoted as MSR-2 and MSR-3, of Aalto were characterized. Second, based on the characterization, a compensation coil set was designed and constructed with the ability for both AC and DC field compensation. Third, the performance of the compensation system was evaluated.

The measurements were performed with a fluxgate magnetometer, which has a maximum noise floor of 10 $\mathrm{pT_{rms}}/\sqrt{\mathrm{Hz}}$; thus, with a bandwidth of 200 Hz, the RMS noise of the fluxgate is 0.14 $\mathrm{nT_{rms}}$. However, the raw fluxgate signals contained much more noise; the standard deviations of the signals were about 0.5 nT. The comparison between the RMS noise level of the fluxgate and the standard deviations of the fluxgate signals suggests that additional sources of noise were present supposedly in the electronics since the high-frequency part of the fluxgate signal is unlikely actual field variation. From this viewpoint, the field excursions calculated from the 10-s time windows can be, to some extent, due to noise, which can explain the similarities between the field excursion histograms. Anyhow, the measured DC fields should have been relatively unaffected by the white noise present in the measurement as they were averages of 10 000 samples. However, the DC measurements could have been affected by other sources of measurement errors and instabilities, e.g., low-frequency drifts of the magnetic field during the measurement as the points were not measured simultaneously and human errors in the positioning of the fluxgate could have happened.

The static magnetic fields inside both of the MSRs were found to be linear to a good extent (taking into account the measurement errors). The ambient fields were on the order of 100 nT in MSR-2 while in MSR-3 they were a magnitude smaller; the largest gradients were about 40 nT/m in MSR-2 and 5 nT/m in MSR-3. Thus, the ambient field in MSR-2 is close to a field in a typical MSR while the field in MSR-3 is remarkably low. Though, the difference between the rooms is not so suprising since the number of layers differs. The field drifts are not so significant in the rooms as the low-frequency field excursions during the 200-s data segments were less than 1.5 nT in both rooms. According to the results, certain types of SERF OPMs could be operated in MSR-3 without any field compensation; though, the sensitivity of the OPMs could be improved further by additional compensation also there. In contrast, in MSR-2, additional compensation is mandatory.

The MSR-2 houses a MEG–MRI system which employs magnetic field pulses up to 30 mT. These pulses can magnetize the walls of the MSR and affect the remanent field inside the MSR. Therefore, the field inside MSR-2 could be possibly decreased by degaussing the walls of the room as, to the author's knowledge, the walls have not been degaussed since the construction of the MSR.

The implemented coil design was chosen because of the high field homogeneity the coils provide and the simulations showed that the coil set was able to reduce the remanent DC fields inside head-sized volumes in the MSRs to an appropriate

level (below 3 nT in MSR-2 and below 1 nT in MSR-3). However, the measured static field compensation performance of the coil system was not as good as expected from the simulations: the measured field amplitudes ranged from 4 to 8 nT with the compensation. These discrepancies between the results are not drastic; few factors can explain them. The initial computer simulations employed 1000 points into which the field amplitudes were interpolated from the experimental data. The large number of points were chosen because accurate estimates for the coil currents were desired and in this sense the optimal performance of the coil set was evaluated. Nonetheless, in an experimental setting, the number of measurement points is limited and thus the estimates of the currents are not necessarily the most accurate; in this case the number of measurement points was seven which is very close to the number of unknowns (the coil currents) that is six. In the experiment, the field and the elements of the current-to-field transfer matrix were measured using an averaging time of 1 s. This rather short window can induce some errors to the matrix elements if the field is drifting during the measurement or if other sources of noise or inaccuracies are present. Also calibration errors between the output voltage of the Elekta system and coil currents may have been present.

The DC-field compensation was only done in MSR-2. It would be interesting to also operate the DC compensation in MSR-3, which has lower field amplitudes, and test whether the results achieved with the simulations could be experimentally replicated. However, MSR-3 is actively used to perform MEG measurements and the operation of the compensation system would require modifications to the software and electronics of the MEG system. Because of the required modifications, it was decided not to alter the MEG system of MSR-3.

The present coil set is only able to compensate the homogeneous components of the field and the diagonal gradients $\partial B_x/\partial x$, $\partial B_y/\partial y$ and $\partial B_z/\partial z$. The compensation coil set could be further enhanced by adding gradient coils that can also compensate the off-diagonal gradients as some of these gradients are non-zero at the MSRs; for example, there is a rather large off-diagonal gradient $\partial B_z/\partial x$ present in the two-layer MSR. Maxwell's equations state that $\nabla \cdot \mathbf{B} = 0$ and $\nabla \times \mathbf{B} = 0$ inside the coil set, which means that only two of the three diagonal gradients and three of the six off-diagonal gradients are independent. For instance, compensation of $\partial B_x/\partial x$ and $\partial B_y/\partial y$ guarantees also compensation of $\partial B_z/\partial z$. Thereby, for a full first-order compensation three additional coil pairs compensating e.g. $\partial B_z/\partial y$, $\partial B_x/\partial z$ and $\partial B_y/\partial x$ would be sufficient.

The AC compensation was tested only by using one magnetometer and nulling the field at its position. This is somewhat trivial and it, in some sense, gives only information about the performance of the feedback loop. This information is, nonetheless, useful since the implementation of the feedback loop and, in particular, the implementation of the digital low-pass filter in it are not obvious. Altogether, it was shown that the feedback loop was able to null the field at the position of the fluxgate sensor sufficiently. However, the AC compensation increased the low-frequency field fluctuations slightly; the field excursion values for the 200-s data, that was low-pass filtered at 1 Hz, were 1.37, 0.60 and 1.74 nT with compensation and 1.12, 0.95 and 1.39 nT without compensation for the x-, y- and z-components

of the field, respectively. The increased fluctuations can be due to various factors. First, the fluxgate as a detector might not be the best solution as the fields are relatively low in the MSRs and noise in the fluxgate is quite high. Second, the digital low-pass filter can cause noise and lag in the compensation signals. Last and most importantly, the tuning of the PI controllers might not be optimal especially for the x- and z-components. However, better tuning and smaller drifts could be potentially achieved since the field drifts with compensation are actually smaller for the y-component. Despite of the increased fluctuations in the 200-s data, the compensation system was able to suppress the even-lower-frequency fluctuations in the 30-min data, which consisted of 10-s averages. For a more interesting performance analysis multiple magnetometers should be used. In this way, field gradients could be also nulled actively and independent detectors could be used to measure the field at multiple positions during the compensation. Anyway, during the time of this thesis only one fluxgate magnetometer was available.

It should be emphasized that the usage of the fluxgate as the magnetic sensor in the compensation set is only temporary as the compensation is intended to be driven by OPMs when they are available. In the final state of the compensation system, the same OPMs will be used to measure both brain responses and the to-be-compensated magnetic noise. The purpose of the 1-Hz low-pass filter is to separate the compensation signal so that only the low frequency drifts of the magnetic field are compensated and the interesting brain signals (> 1 Hz) remain intact. Thus, the actual dynamic performance of the system will become evident when OPMs are available. This thesis showed that the feedback loop functions and is feasible but questions concerning mainly the digital filter remain: whether this filter is able to separate the field drifts from the brain responses and whether, e.g., the lag of the filter is acceptable. If the filter does not perform as expected, other methods are needed. For example, the input of the filter could be downsampled from 10 kHz to a smaller frequency; this would allow the usage of a filter with much wider normalized pass-band. Additionally, methods that can spatially uncover the compensation-field-disturbed brain responses could be developed and used; in SQUID-based active compensation, the signal space separation method [65] has been succesfully used [60].

6 Conclusions

This work showed that with the developed hardware sensitive biomagnetic measurements with optically-pumped magnetometers should be feasible in the magnetically shielded rooms of Aalto University. To decrease the magnetic field amplitudes in the rooms, a portable compensation system was designed and constructed and the system was verified to be capable both for static and dynamic field compensation. The feedback loop of the compensation system allows the compensation to be driven flexibly with a number of sensors of different types. Depending on the characteristics of the optically-pumped magnetometer, i.e., the limits for field amplitudes and drifts, the measurement setup may be configured to meet the needs by choosing the right room and by selecting the locations of the sensors so that active homogeneous and gradient field compensation can be provided.

References

[1] M. Hämäläinen, R. Hari, R. J. Ilmoniemi, J. Knuutila, and O. V. Lounasmaa, "Magnetoencephalography—theory, instrumentation, and applications to noninvasive studies of the working human brain," *Reviews of modern Physics*, vol. 65, no. 2, p. 413, 1993.

[2] P. Hansen, M. Kringelbach, and R. Salmelin, *MEG: An introduction to methods*. Oxford university press, 2010.

[3] D. Budker and M. Romalis, "Optical magnetometry," *Nature Physics*, vol. 3, no. 4, pp. 227–234, 2007.

[4] D. Budker and D. F. J. Kimball, *Optical magnetometry*. Cambridge University Press, 2013.

[5] V. K. Shah and R. T. Wakai, "A compact, high performance atomic magnetometer for biomedical applications," *Physics in medicine and biology*, vol. 58, no. 22, p. 8153, 2013.

[6] O. Alem, A. M. Benison, D. S. Barth, J. Kitching, and S. Knappe, "Magnetoencephalography of epilepsy with a microfabricated atomic magnetrode," *The Journal of Neuroscience*, vol. 34, no. 43, pp. 14324–14327, 2014.

[7] I. Kominis, T. Kornack, J. Allred, and M. Romalis, "A subfemtotesla multichannel atomic magnetometer," *Nature*, vol. 422, no. 6932, pp. 596–599, 2003.

[8] T. Sander, J. Preusser, R. Mhaskar, J. Kitching, L. Trahms, and S. Knappe, "Magnetoencephalography with a chip-scale atomic magnetometer," *Biomedical optics express*, vol. 3, no. 5, pp. 981–990, 2012.

[9] C. N. Johnson, P. Schwindt, and M. Weisend, "Multi-sensor magnetoencephalography with atomic magnetometers," *Physics in medicine and biology*, vol. 58, no. 17, p. 6065, 2013.

[10] K. Kim, S. Begus, H. Xia, S.-K. Lee, V. Jazbinsek, Z. Trontelj, and M. V. Romalis, "Multi-channel atomic magnetometer for magnetoencephalography: A configuration study," *NeuroImage*, vol. 89, pp. 143–151, 2014.

[11] D. M. Goldenholz, S. P. Ahlfors, M. S. Hämäläinen, D. Sharon, M. Ishitobi, L. M. Vaina, and S. M. Stufflebeam, "Mapping the signal-to-noise-ratios of cortical sources in magnetoencephalography and electroencephalography," *Human brain mapping*, vol. 30, no. 4, pp. 1077–1086, 2009.

[12] M. F. Bear, B. W. Connors, and M. A. Paradiso, *Neuroscience*, vol. 2. Lippincott Williams & Wilkins, 2007.

[13] L. L. Iversen, "The chemistry of the brain," *Scientific American*, vol. 241, no. 3, pp. 134–49, 1979.

[14] S. Murakami and Y. Okada, "Contributions of principal neocortical neurons to magnetoencephalography and electroencephalography signals," *The Journal of physiology*, vol. 575, no. 3, pp. 925–936, 2006.

[15] M. Stenroos *et al.*, *Boundary element method in spatial characterization of the electrocardiogram*. Teknillinen korkeakoulu, 2008.

[16] A. S. Ferguson and G. Stroink, "Factors affecting the accuracy of the boundary element method in the forward problem. I. Calculating surface potentials," *Biomedical Engineering, IEEE Transactions on*, vol. 44, no. 11, pp. 1139–1155, 1997.

[17] M. Stenroos, V. Mäntynen, and J. Nenonen, "A Matlab library for solving quasi-static volume conduction problems using the boundary element method," *Computer methods and programs in biomedicine*, vol. 88, no. 3, pp. 256–263, 2007.

[18] D. B. Geselowitz, "On the magnetic field generated outside an inhomogeneous volume conductor by internal current sources," *Magnetics, IEEE Transactions on*, vol. 6, no. 2, pp. 346–347, 1970.

[19] M. S. Hamalainen and J. Sarvas, "Realistic conductivity geometry model of the human head for interpretation of neuromagnetic data," *Biomedical Engineering, IEEE Transactions on*, vol. 36, no. 2, pp. 165–171, 1989.

[20] M. Stenroos and J. Sarvas, "Bioelectromagnetic forward problem: isolated source approach revis (it) ed," *Physics in medicine and biology*, vol. 57, no. 11, p. 3517, 2012.

[21] B. D. Josephson, "Possible new effects in superconductive tunnelling," *Physics letters*, vol. 1, no. 7, pp. 251–253, 1962.

[22] V. Shah and M. Romalis, "Spin-exchange relaxation-free magnetometry using elliptically polarized light," *Physical Review A*, vol. 80, no. 1, p. 013416, 2009.

[23] V. Shah, S. Knappe, P. D. Schwindt, and J. Kitching, "Subpicotesla atomic magnetometry with a microfabricated vapour cell," *Nature Photonics*, vol. 1, no. 11, pp. 649–652, 2007.

[24] W. Happer, "Optical pumping," *Reviews of Modern Physics*, vol. 44, no. 2, p. 169, 1972.

[25] J. Allred, R. Lyman, T. Kornack, and M. Romalis, "High-sensitivity atomic magnetometer unaffected by spin-exchange relaxation," *Physical review letters*, vol. 89, no. 13, p. 130801, 2002.

[26] S. Appelt, A. B.-A. Baranga, C. Erickson, M. Romalis, A. Young, and W. Happer, "Theory of spin-exchange optical pumping of 3 He and 129 Xe," *Physical Review A*, vol. 58, no. 2, p. 1412, 1998.

[27] S. Seltzer and M. Romalis, "Unshielded three-axis vector operation of a spin-exchange-relaxation-free atomic magnetometer," *Applied physics letters*, vol. 85, no. 20, pp. 4804–4806, 2004.

[28] M. Auzinsh, D. Budker, D. Kimball, S. Rochester, J. Stalnaker, A. Sushkov, and V. Yashchuk, "Can a quantum nondemolition measurement improve the sensitivity of an atomic magnetometer?," *Physical review letters*, vol. 93, no. 17, p. 173002, 2004.

[29] M. Ledbetter, I. Savukov, V. Acosta, D. Budker, and M. Romalis, "Spin-exchange-relaxation-free magnetometry with Cs vapor," *Physical Review A*, vol. 77, no. 3, p. 033408, 2008.

[30] H. Robinson, E. Ensberg, and H. Dehmelt, "Preservation of spin state in free atom-inert surface collisions," *Bull. Am. Phys. Soc*, vol. 3, no. 9, 1958.

[31] M. Balabas, T. Karaulanov, M. Ledbetter, and D. Budker, "Polarized alkali-metal vapor with minute-long transverse spin-relaxation time," *Physical review letters*, vol. 105, no. 7, p. 070801, 2010.

[32] J. O. Hirschfelder, C. F. Curtiss, R. B. Bird, and M. G. Mayer, *Molecular theory of gases and liquids*, vol. 26. Wiley New York, 1954.

[33] W. Happer and H. Tang, "Spin-exchange shift and narrowing of magnetic resonance lines in optically pumped alkali vapors," *Physical Review Letters*, vol. 31, no. 5, p. 273, 1973.

[34] W. Happer and A. Tam, "Effect of rapid spin exchange on the magnetic-resonance spectrum of alkali vapors," *Physical Review A*, vol. 16, no. 5, p. 1877, 1977.

[35] W. Happer and B. Mathur, "Effective operator formalism in optical pumping," *Physical Review*, vol. 163, no. 1, p. 12, 1967.

[36] I. Novikova, A. Matsko, V. Velichansky, M. O. Scully, and G. R. Welch, "Compensation of ac Stark shifts in optical magnetometry," *Physical Review A*, vol. 63, no. 6, p. 063802, 2001.

[37] P. D. Schwindt, S. Knappe, V. Shah, L. Hollberg, J. Kitching, L.-A. Liew, and J. Moreland, "Chip-scale atomic magnetometer," *Applied Physics Letters*, vol. 85, no. 26, pp. 6409–6411, 2004.

[38] S. Knappe, T. Sander, and L. Trahms, "Optically-pumped magnetometers for MEG," in *Magnetoencephalography*, pp. 993–999, Springer, 2014.

[39] S. Knappe, V. Gerginov, P. Schwindt, V. Shah, H. Robinson, L. Hollberg, and J. Kitching, "Atomic vapor cells for chip-scale atomic clocks with improved long-term frequency stability," *Optics Letters*, vol. 30, no. 18, pp. 2351–2353, 2005.

[40] W. C. Griffith, S. Knappe, and J. Kitching, "Femtotesla atomic magnetometry in a microfabricated vapor cell," *Optics express*, vol. 18, no. 26, pp. 27167–27172, 2010.

[41] P. D. Schwindt, B. Lindseth, S. Knappe, V. Shah, J. Kitching, and L.-A. Liew, "Chip-scale atomic magnetometer with improved sensitivity by use of the Mx technique," *Applied Physics Letters*, vol. 90, no. 8, pp. 081102–081102, 2007.

[42] R. R. Mhaskar, S. Knappe, and J. Kitching, "Low-frequency characterization of MEMS-based portable atomic magnetometer," in *Frequency Control Symposium (FCS), 2010 IEEE International*, pp. 376–379, IEEE, 2010.

[43] J. Preusser, S. Knappe, J. Kitching, and V. Gerginov, "A microfabricated photonic magnetometer," in *Frequency Control Symposium, 2009 Joint with the 22nd European Frequency and Time forum. IEEE International*, pp. 1180–1182, IEEE, 2009.

[44] S. Celozzi, G. Lovat, and R. Araneo, *Electromagnetic shielding*. Wiley Online Library, 2008.

[45] NEC/TOCIN, *Product catalog*. http://www.nec-tokin.com/english/product/pdf_dl/magnetic_shielding_chamber.pdf.

[46] V. O. Kelhä, J. M. Pukki, R. S. Peltonen, A. J. Penttinen, R. J. Ilmoniemi, and J. J. Heino, "Design, construction, and performance of a large-volume magnetic shield," *Magnetics, IEEE Transactions on*, vol. 18, no. 1, pp. 260–270, 1982.

[47] V. O. Kelhä, R. Peltonen, and B. Rantala, "The effect of shaking on magnetic shields," *Magnetics, IEEE Transactions on*, vol. 16, no. 4, pp. 575–578, 1980.

[48] H. Ter Brake, H. Wieringa, and H. Rogalla, "Improvement of the performance of a mu-metal magnetically shielded room by means of active compensation (biomagnetic applications)," *Measurement Science and Technology*, vol. 2, no. 7, p. 596, 1991.

[49] J. Bork, H. Hahlbohm, R. Klein, and A. Schnabel, "The 8-layered magnetically shielded room of the PTB: Design and construction," in *Biomag2000, Proc. 12th Int. Conf. on Biomagnetism*, pp. 970–73, Espoo, Finland, 2001.

[50] H. Xia, A. B.-A. Baranga, D. Hoffman, and M. Romalis, "Magnetoencephalography with an atomic magnetometer," *Applied Physics Letters*, vol. 89, no. 21, p. 211104, 2006.

[51] O. Alem, T. H. Sander, R. Mhaskar, J. LeBlanc, H. Eswaran, U. Steinhoff, Y. Okada, J. Kitching, L. Trahms, and S. Knappe, "Fetal magnetocardiography measurements with an array of microfabricated optically pumped magnetometers," *Physics in medicine and biology*, vol. 60, no. 12, p. 4797, 2015.

[52] C. Johnson and P. D. Schwindt, "A two-color pump probe atomic magnetometer for magnetoencephalography," in *Frequency Control Symposium (FCS), 2010 IEEE International*, pp. 371–375, IEEE, 2010.

[53] R. Wyllie, M. Kauer, G. Smetana, R. Wakai, and T. Walker, "Magnetocardiography with a modular spin-exchange relaxation-free atomic magnetometer array," *Physics in medicine and biology*, vol. 57, no. 9, p. 2619, 2012.

[54] Bartington Instruments, *Mag-03 Three-Axis Magnetic Field Sensors*. http://www.bartington.com/Literaturepdf/Datasheets/Mag-03%20DS0013.pdf.

[55] T. Kugelstadt, "Active filter design techniques," in *Op Amps for Everyone: Design Reference*, pp. 271–281, 2008.

[56] K. Zevenhoven, "Performance of sensor arrays for SQUID-detected MRI of the brain," *Special assignment, Aalto University, Finland*, 2009.

[57] D. Platzek, H. Nowak, F. Giessler, J. Röther, and M. Eiselt, "Active shielding to reduce low frequency disturbances in direct current near biomagnetic measurements," *Review of scientific instruments*, vol. 70, no. 5, pp. 2465–2470, 1999.

[58] H. Nowak, J. Haueisen, M. Ziolkowski, F. Resmer, J. Schüler, and F. Gießler, "Active shielding in measurements of DC near biomagnetic fields," in *Engineering in Medicine and Biology Society, 2001. Proceedings of the 23rd Annual International Conference of the IEEE*, vol. 4, pp. 3277–3280, IEEE, 2001.

[59] C. Gu, S. Zou, Z. Han, and T.-M. Qu, "Passive magnetic field cancellation device by multiple high-Tc superconducting coils," *Review of Scientific Instruments*, vol. 81, no. 4, p. 045101, 2010.

[60] S. Taulu, J. Simola, J. Nenonen, and L. Parkkonen, "Novel noise reduction methods," in *Magnetoencephalography*, pp. 35–71, Springer, 2014.

[61] A. H. Firester, "Design of square Helmholtz coil systems," *Review of Scientific Instruments*, vol. 37, no. 9, pp. 1264–1265, 1966.

[62] J. L. Kirschvink, "Uniform magnetic fields and double-wrapped coil systems: improved techniques for the design of bioelectromagnetic experiments," *Bioelectromagnetics*, vol. 13, no. 5, pp. 401–411, 1992.

[63] J. Ditterich and T. Eggert, "Improving the homogeneity of the magnetic field in the magnetic search coil technique," *Biomedical Engineering, IEEE Transactions on*, vol. 48, no. 10, pp. 1178–1185, 2001.

[64] J. Kauraniemi, T. I. Laakso, I. Hartimo, and S. J. Ovaska, "Delta operator realizations of direct-form IIR filters," *Circuits and Systems II: Analog and Digital Signal Processing, IEEE Transactions on*, vol. 45, no. 1, pp. 41–52, 1998.

[65] S. Taulu, M. Kajola, and J. Simola, "Suppression of interference and artifacts by the signal space separation method," *Brain topography*, vol. 16, no. 4, pp. 269–275, 2004.

[66] R. H. Middleton and G. C. Goodwin, "Improved finite word length characteristics in digital control using delta operators," *Automatic Control, IEEE Transactions on*, vol. 31, no. 11, pp. 1015–1021, 1986.

[67] A. Kojo, "A versatile low-noise downsampler for a magnetoencephalography system," *Master's thesis, Aalto University, Finland*, 2008.

A Delta operator direct-form IIR filters

In digital control, a fast sampling rate relative to signal bandwidth is commonly used. Thus, very narrow pass-band low-pass filters are needed. However, the number of bits available for representing filter coefficients and for performing arithmetics is limited; the quantizations thereby cause finite-word-length effects such as roundoff noise in the digital implementation of filters. To cope with these effects, various methods have been introduced.

The finite-word-length performance of the filter is often enhanced by using cascaded filter implementations where the filter is realized using a sequence of second-order filter blocks. The transfer function of a cascaded filter is

$$H(z) = g \prod_{i=0}^{m} H_i(z), \tag{A1}$$

where g is the overall gain, z is the delay operator and $H_i(z)$ is the transfer function of one section:

$$H_i(z) = \frac{b_{0i} + b_{1i}z^{-1} + b_{2i}z^{-2}}{1 + a_{1i}z^{-1} + a_{2i}z^{-2}}. \tag{A2}$$

Numerous filter constructions to reduce finite-word-length effects have been introduced, of which delta operator filter realizations are prominent. The advantages of the delta operator compared to delay-operator realizations include [66]

- superior finite-word-length coefficient representation,
- superior finite-word-length rounding error performance,
- superior numerical properties in calculations with discrete models,
- convergence of discrete-time results and models to their continuous counterparts as the sampling rate is increased.

The delta operator is obtained by substituting the forward shift operator z by [66]

$$\delta = \frac{z - 1}{\Delta}, \tag{A3}$$

where Δ is the sampling interval; however, it can be viewed also as a free optimizable parameter [64]. The delta operator form of a cascaded filter is [64]

$$H(\delta) = g \prod_{i=0}^{m} \frac{\beta_{0i} + \beta_{1i}\delta^{-1} + \beta_{2i}\delta^{-2}}{1 + \alpha_{1i}\delta^{-1} + \alpha_{2i}\delta^{-2}}, \tag{A4}$$

where the filter coefficients are given by

$$\beta_{0k} = b_{0k} \qquad \alpha_{0k} = 1 \tag{A5}$$

$$\beta_{1k} = \frac{2b_{0k} + b_{1k}}{\Delta_k} \qquad \alpha_{1k} = \frac{2 + a_{1k}}{\Delta_k} \tag{A6}$$

$$\beta_{2k} = \frac{b_{0k} + b_{1k} + b_{2k}}{\Delta_k^2} \qquad \alpha_{1k} = \frac{1 + a_{1k} + a_{2k}}{\Delta_k^2}. \tag{A7}$$

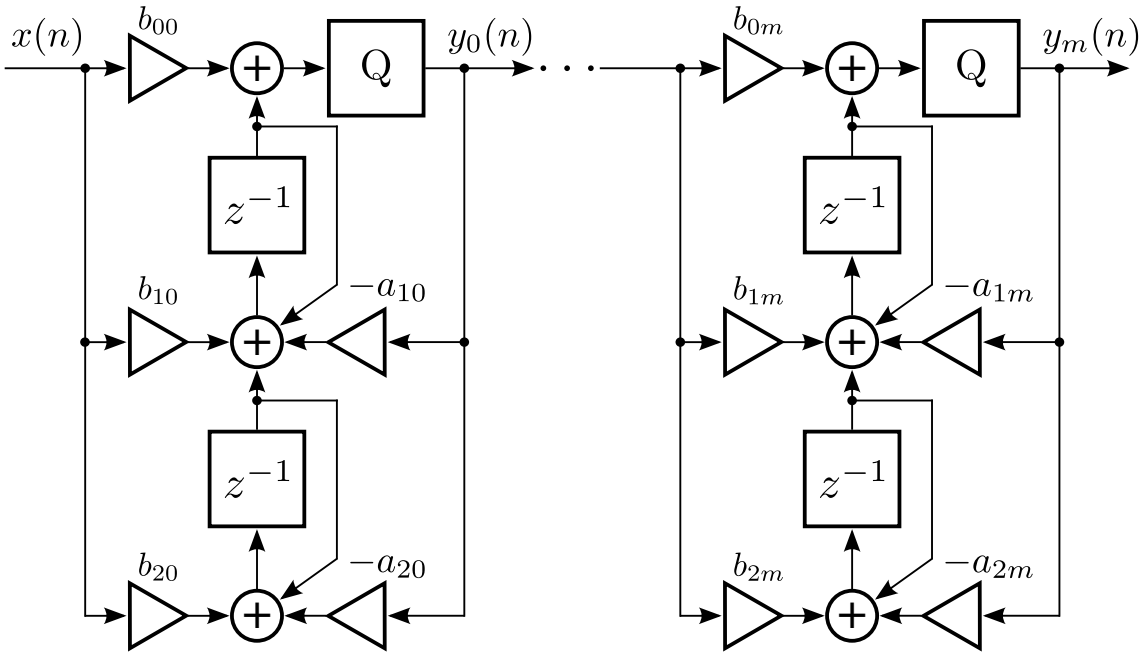

Figure A1: Signal flow chart for a direct-form II transposed delta operator IIR filter. The filter is composed of $m + 1$ second-order sections. Quantization is denoted with Q and z is the delay operator. Figure is inspired by Ref. 67.

The numerical performance of the filter can be further modified by changing the order of operations in the filter implementation as the order does not affect the filter transfer function. The filters are thus often described with signal flow charts which give the order of the operations on the samples. In digital filtering, the most commonly used structures, which indicate the sequence ordering, are so-called direct-form (DF) structures.

The finite-word-length performance of a digital filter can thus be controlled with various choices of structures and parameters. Kauraniemi and colleagues [64] analyzed the roundoff noise performance of several delta operator IIR filter implementations; the filters were composed of second-order sections, and different DF structures were tested. They found that of all the DF structures the direct form II transposed (DFIIt) performed best with respect to the quantization noise. They also stated that when double-precision inverse delta operations are used, the optimum noise performance is obtained with $\Delta = 1$. They concluded that with a DFIIt delta-operator IIR filter excellent roundoff noise performance is achieved at the cost of only a minor additional implementation complexity when compared with the corresponding delay realization. The signal flow chart of the DFIIt delta operator IIR filter is represented in Fig. A1.